

Small-molecule inhibition of SARS-CoV-2 NSP14 RNA cap methyltransferase

<https://doi.org/10.1038/s41586-024-08320-0>

Received: 22 November 2023

Accepted: 31 October 2024

Published online: 11 December 2024

 Check for updates

Cindy Meyer¹, Aitor Garzia¹, Michael W. Miller², David J. Huggins^{2,3}, Robert W. Myers², Hans-Heinrich Hoffmann⁴, Alison W. Ashbrook⁴, Syeda Y. Jannath⁴, Nigel Liverton², Stacia Kargman², Matthew Zimmerman⁵, Andrew M. Nelson⁵, Vijeta Sharma⁵, Enriko Dolgov⁵, Julianna Cangialosi⁵, Suyapa Penalva-Lopez⁵, Nadine Alvarez⁵, Ching-Wen Chang^{4,5,6}, Neelam Oswal⁵, Irene Gonzalez⁵, Risha Rasheed⁵, Kira Goldgirsh⁵, Jada A. Davis¹, Lavoisier Ramos-Espiritu⁷, Miriam-Rose Menezes⁷, Chloe Larson⁷, Julius Nitsche⁸, Oleg Ganichkin⁸, Hanan Alwaseem⁹, Henrik Molina⁹, Stefan Steinbacher⁸, J. Fraser Glickman⁷, David S. Perlin⁵, Charles M. Rice⁴, Peter T. Meinke² & Thomas Tuschl¹ 

Coronavirus disease 2019 (COVID-19) is caused by severe acute respiratory syndrome coronavirus 2 (SARS-CoV-2)¹. The rapid development of highly effective vaccines^{2,3} against SARS-CoV-2 has altered the trajectory of the pandemic, and antiviral therapeutics⁴ have further reduced the number of COVID-19 hospitalizations and deaths. Coronaviruses are enveloped, positive-sense, single-stranded RNA viruses that encode various structural and non-structural proteins, including those critical for viral RNA replication and evasion from innate immunity⁵. Here we report the discovery and development of a first-in-class non-covalent small-molecule inhibitor of the viral guanine-N7 methyltransferase (MTase) NSP14. High-throughput screening identified RU-0415529, which inhibited SARS-CoV-2 NSP14 by forming a unique ternary S-adenosylhomocysteine (SAH)-bound complex. Hit-to-lead optimization of RU-0415529 resulted in TDI-015051 with a dissociation constant (K_d) of 61 pM and a half-maximal effective concentration (EC_{50}) of 11 nM, inhibiting virus infection in a cell-based system. TDI-015051 also inhibited viral replication in primary small airway epithelial cells and in a transgenic mouse model of SARS CoV-2 infection with an efficacy comparable with the FDA-approved reversible covalent protease inhibitor nirmatrelvir⁶. The inhibition of viral cap methylases as an antiviral strategy is also adaptable to other pandemic viruses.

Coronaviruses encode their own MTases to synthesize cap-0 and cap-1 on their viral mRNA to promote translation and evade innate immunity, respectively^{7–11}. These MTases are unrelated to human proteins, making them excellent targets for the development of small-molecule inhibitors¹².

Development of TDI-015051

At the onset of the SARS-CoV-2 pandemic in 2020, we conducted high-throughput screening for inhibiting the guanine-N7 MTase activity of full-length SARS-CoV-2 NSP14 (Extended Data Fig. 1a,b) in 384-well format using a luminescence-based readout (Extended Data Fig. 1c). The Michaelis–Menten constants (K_m) for GpppA and S-adenosylmethionine (SAM) were 0.65 μM and 1.71 μM, respectively (Fig. 1a–c). The screen used 15 nM NSP14, 1 μM GpppA cap and 2 μM methyl donor SAM. Sinefungin, a broad-spectrum MTase inhibitor and SAM analogue¹³, served as a positive control for NSP14 inhibition. A replicate pilot screen of 1,268 pharmacologically active compounds showed assay reproducibility with an

R^2 value of 0.95 (Fig. 1d). We then screened 430,376 unique compounds at a concentration of 25 μM (Fig. 1e), obtaining an average Z' value of 0.88 ± 0.04 ($n = 1,312$ plates; Extended Data Fig. 1d), and identified 378 compounds with more than 60 normalized percent inhibition (NPI).

After various counter screens, 57 hits remained, 28 of which showed an half-maximal inhibitory concentration (IC_{50}) ≤ 10 μM following dose–response evaluation. We selected RU-0415529 ($IC_{50} = 356$ nM; Fig. 1f) for further characterization and medicinal chemistry hit-to-lead optimization. After 16 rounds of iterative chemical modification, IC_{50} values improved 1,000-fold, enabling cell-based functional testing. Over the next six rounds, potency and pharmacological properties were further enhanced, resulting in TDI-015051 ($IC_{50} \leq 0.15$ nM; Fig. 1f), a compound suitable for animal model proof-of-concept testing.

NSP14–SAH–TDI-015051 inhibitory complex

We measured the IC_{50} values of RU-0415529 and sinefungin as a function of GpppA and SAM substrate concentrations (Extended

¹Laboratory for RNA Molecular Biology, The Rockefeller University, New York, NY, USA. ²Sanders Tri-Institutional Therapeutics Discovery Institute, The Rockefeller University, New York, NY, USA.

³Department of Physiology and Biophysics, Weill Cornell Medical College, New York, NY, USA. ⁴Laboratory of Virology and Infectious Disease, The Rockefeller University, New York, NY, USA.

⁵Center for Discovery and Innovation, Hackensack Meridian Health, Nutley, NJ, USA. ⁶Department of Medicine, Division of Infectious Diseases, Columbia University, New York, NY, USA. ⁷Fisher Drug Discovery Resource Center, The Rockefeller University, New York, NY, USA. ⁸PROTEROS Biostructures GmbH, Planegg-Martinsried, Germany. ⁹Proteomics Resource Center, The Rockefeller University, New York, NY, USA. [✉]e-mail: ttuschl@rockefeller.edu

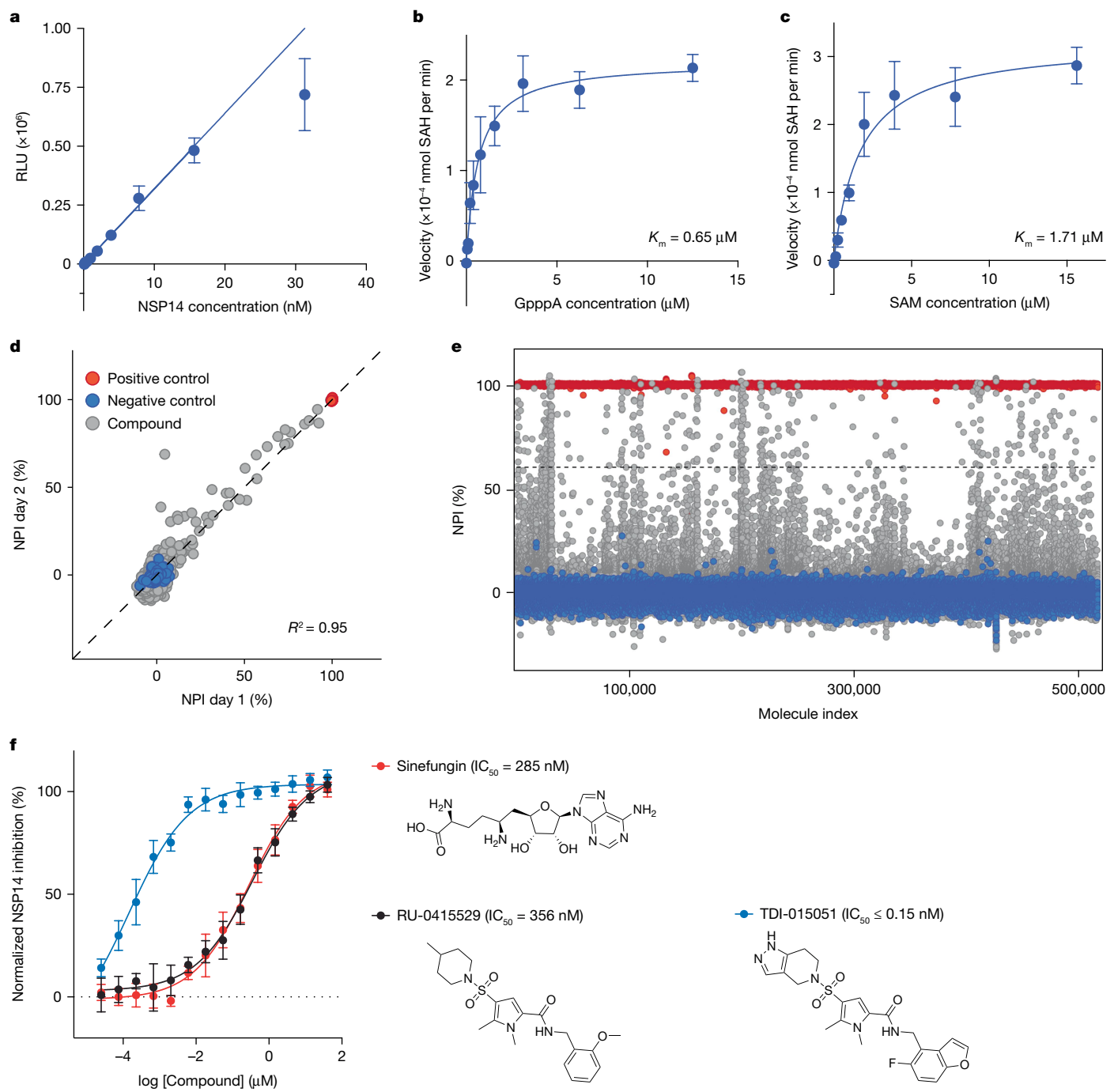


Fig. 1 | Identification of RU-0415529 and the development of TDI-015051. **a**, Biochemical MTase activity assay of SARS-CoV-2 NSP14 (0–32 nM) at near-saturating conditions of GpppA (10 μM) and SAM (10 μM) using the MTase Glo assay for detection. RLU, relative luminescence units. $n = 3$. Data are shown as mean ± s.d. **b**, Titration of GpppA at 15 nM NSP14 and 10 μM SAM for K_m value determination. $n = 3$. Data are shown as mean ± s.d. **c**, Titration of SAM at 15 nM NSP14 and 10 μM GpppA for K_m value determination. $n = 3$. Data are shown as mean ± s.d. **d**, Pharmacologically active compounds ($n = 1,268$; 25 μM each) were tested for NSP14 inhibition on 2 different days. A correlation of NPI for each tested compound (grey dots) is shown. The blue dots indicate DMSO-negative controls, and the red dots indicate positive controls (100 μM sinefungin). **e**, Fisher Drug Discovery Resource Center compound library (430,376 unique compounds; grey dots) screened at 25 μM for NSP14 inhibition given as NPI for each tested compound (grey dots). The molecule index indicates the unique number assigned to each compound in the library. The blue dots indicate DMSO-negative control, and the red dots indicate positive control (100 μM sinefungin). The horizontal dotted line indicates an NPI ≥ 60 used as a threshold for hit identification. **f**, Dose-dependent inhibition of SARS-CoV-2 NSP14 by sinefungin, RU-0415529 and TDI-015051 tested under low enzyme concentration conditions (0.3 nM NSP14, 3 μM GpppA and 5 μM SAM). The horizontal dotted line indicates an NPI = 0. Chemical structures and IC_{50} values of compounds are indicated. $n = 3$. Data are shown as mean ± s.d.

e, Fisher Drug Discovery Resource Center compound library (430,376 unique compounds; grey dots) screened at 25 μM for NSP14 inhibition given as NPI for each tested compound (grey dots). The molecule index indicates the unique number assigned to each compound in the library. The blue dots indicate DMSO-negative control, and the red dots indicate positive control (100 μM sinefungin). The horizontal dotted line indicates an NPI ≥ 60 used as a threshold for hit identification. **f**, Dose-dependent inhibition of SARS-CoV-2 NSP14 by sinefungin, RU-0415529 and TDI-015051 tested under low enzyme concentration conditions (0.3 nM NSP14, 3 μM GpppA and 5 μM SAM). The horizontal dotted line indicates an NPI = 0. Chemical structures and IC_{50} values of compounds are indicated. $n = 3$. Data are shown as mean ± s.d.

Data Fig. 2a). Sinefungin showed SAM-competitive behaviour, and its IC_{50} value was also enhanced by increasing GpppA concentration. The IC_{50} values for RU-0415529 inhibiting NSP14 did not change as a function of SAM or GpppA concentration, indicating

a non-competitive mechanism of inhibition with respect to SAM and GpppA.

A combination of biophysical methods revealed the inhibitory mechanism of NSP14 by RU-0415529 and TDI-015051. Protein denaturation

thermal shift assays did not detect a melting temperature (T_m) shift for NSP14 when incubated individually with SAM, GpppA, m⁷GpppA, sinefungin, RU-0415529 or TDI-015051 (Extended Data Fig. 2b,c). However, addition of SAH increased the T_m of NSP14 from 50.2 °C to 54.6 °C (Fig. 2a and Extended Data Fig. 2b,c), which further increased to 56.0 °C, 60.2 °C or 73.0 °C upon addition of m⁷GpppA, RU-0415529 or TDI-015051, respectively. No further change in the T_m of the NSP14–SAH complex was observed when GpppA was added. Therefore, the products of cap methylation, rather than its substrates, are bound to NSP14 as a ternary complex. The much larger increase in T_m of the NSP14–SAH complex upon TDI inhibitor binding suggested that the inhibitor occupies the SAH-stabilized cap-binding pocket of NSP14, forming additional stabilizing interactions.

Surface plasmon resonance showed binding of SAH to NSP14 with an association rate (k_a) of $3.9 \times 10^6 \text{ M}^{-1} \text{ s}^{-1}$ and a dissociation rate (k_d) of $8.7 \times 10^{-2} \text{ s}^{-1}$, yielding a dissociation constant (K_d) of 23 nM (Extended Data Fig. 2d). In the presence of 10 μM SAH, TDI-015051 bound to NSP14 with a K_d of 61 pM based on a k_a of $1.3 \times 10^6 \text{ M}^{-1} \text{ s}^{-1}$ and a low k_d of $7.8 \times 10^{-5} \text{ s}^{-1}$ (Fig. 2b), indicating a highly stable inhibitory ternary complex.

Molecular docking and free energy calculations using the SARS-CoV-2 NSP14–SAH structure 7R2V¹⁴ and compared with the SARS-CoV-1 NSP14–SAH–GpppA structure 5C8S¹⁵ further predicted that TDI-015051 occupied the guanine cap-binding pocket of the MTase domain in contact with SAH. We subsequently solved a co-crystal structure of the ternary NSP14–SAH–TDI-015051 complex at 2.18 Å (Fig. 2c–f and Extended Data Tables 1 and 2), confirming that TDI-015051 occupied the cap-binding pocket of the MTase domain, adjacent to the SAH (and SAM)-binding site. The exocyclic pyrazole group of TDI-015051 is located at the position of the guanine ring (Extended Data Fig. 2e), thereby preventing cap substrate binding and its methylation. The NSP14 structure was very similar to previously solved structures of NSP14 from SARS-CoV-1 (refs. 15,16) and SARS-CoV-2 (refs. 14,17–19). Comparison of NSP14 structures in the presence and absence of SAH revealed that residues Asp352 to Phe377 rearranged to form a lid, which buries SAH and TDI-015051, explaining the requirement of co-binding of the inhibitor and SAH and the very slow dissociation of the complex (Fig. 2d). A significant portion of TDI-015051 directly contacted SAH, including an amide hydrogen bond to the SAH carboxylate group. In addition, the fluoro-benzofuran group of TDI-015051 stacked on top of a salt bridge between Arg310 and the SAH carboxylate. Such stacking interactions can be very strong²⁰ and require the presence of SAH. Finally, a hydrogen bonding interaction of the sulfonamide group with Asn386 and deep burial of the exocyclic pyrazole group in the hydrophobic cap-binding site contributed to compound binding. The large increase in affinity from RU-0415529 to TDI-015051 can be explained by three factors: first, the fluoro-benzofuran in TDI-015051 is expected to exhibit improved stacking on the Arg310–SAH salt bridge relative to the methoxy-phenyl group in RU-0415529; second, the exocyclic pyrazole group in TDI-015051 fills the cap-binding pocket more completely than the methyl-piperidine in RU-0415529; and third, the exocyclic pyrazole group forms an additional hydrogen bond with Thr428 that is absent in RU-0415529. Enzyme inhibition by formation of a ternary complex with a reaction product, here SAH, and with an inhibitor mimicking the second reaction product, here RU-0415529 or TDI-015051, respectively, has rarely been found^{21,22}.

Cell-based activity of TDI-015051

Although the original screening hit RU-0415529 did not yet show anti-viral activity in Huh-7.5 cells (Extended Data Fig. 3a), the more potent TDI-015051 inhibited SARS-CoV-2 infection with an EC₅₀ of 11.4 nM; no cytotoxicity was detected at tested concentrations of 3 μM or lower (Fig. 3a).

Untreated Huh-7.5 cells had intracellular concentrations of SAM and SAH of 29.4 μM and 3.9 μM, respectively, as quantified by mass spectrometry (Extended Data Fig. 3b). We questioned whether these intracellular concentrations were optimal for NSP14 inhibition. To increase intracellular SAH, we treated Huh-7.5 cells with 3-deazaneplanocin A (DZNeP), which inhibits S-adenosylhomocysteinase (AHCY), the only enzyme in mammals that catalyses the hydrolysis of SAH into adenosine and homocysteine^{23,24}. Although intracellular SAM remained largely unaffected by 5 μM DZNeP, intracellular SAH increased 31-fold to 121.9 μM (Extended Data Fig. 3b). Consequently, co-treatment of Huh-7.5 cells with 5 μM DZNeP further potentiated TDI-015051 antiviral activity (EC₅₀ = 0.8 nM; Fig. 3a), providing direct evidence that ternary complex formation drives NSP14 inhibition intracellularly. The addition of SAH to cell culture media did not increase cell-based antiviral activity of TDI-015051 (Extended Data Fig. 3c).

We then tested more biologically relevant cell types of SARS-CoV-2 infection and found that TDI-015051 potently inhibited viral infection in the adenocarcinoma-derived alveolar basal epithelial cell line A549 expressing ACE2 and TMPRSS2 (EC₅₀ = 64.7 nM; Extended Data Fig. 3d). At concentrations of 4 nM and above, TDI-015051 also prevented SARS-CoV-2 viral replication in human primary small airway epithelial cells grown at the air–liquid interface as revealed by tissue culture infectious dose (TCID₅₀) assays (Fig. 3b).

Resistance mutations to TDI-015051

Next, we focused on the development of SARS-CoV-2 resistance to TDI-015051 using Vero E6 cells, which are highly permissive for SARS-CoV-2 infection²⁵. We first confirmed that 1 h pre-treatment of Vero E6 cells with TDI-015051 inhibited SARS-CoV-2 infection, when cells were fixed 24 h, 48 h or 72 h after virus treatment, with EC₅₀ values of 99.5 nM, 71.1 nM or 52.4 nM, respectively (Extended Data Fig. 4a). SARS-CoV-2 was then passaged in Vero E6 cells either in the presence of dimethylsulfoxide (DMSO; control, three lineages) or TDI-015051, whose concentration was stepwise increased over five passages from 1× EC₈₅ to 25× EC₈₅ (three lineages) or from 1× EC₉₈ to 25× EC₉₈ (two lineages), respectively (Extended Data Fig. 4b). After five passages, DMSO-treated lineages remained highly sensitive to TDI-015051 (EC₅₀ between 42.3 nM and 62.6 nM; Fig. 3c). However, all TDI-015051-treated lineages demonstrated increased resistance with EC₅₀ values elevated up to 160-fold for the EC₈₅-passaged lineages or up to 290-fold for the EC₉₈-passaged lineages relative to the starting virus (Fig. 3d and Extended Data Fig. 4c).

Total RNA was isolated and sequenced from the cell supernatants after each passage (Fig. 3e and Extended Data Fig. 4d). After five passages, seven distinct mutations were identified in the three EC₈₅ lineages, with P335S being dominant. N306K, N306S, P335S, P335H and H424R were located in the MTase domain. V290A was located in the short hinge region connecting the ExoN and MTase domains²⁶ and directed towards the SAM-binding and RNA-binding pockets (Fig. 3f). S503T was not located in proximity to the substrate-binding pockets. For lineages, in which viruses were initially selected with a TDI-015051 concentration of EC₉₈, the P335S mutation was the dominant mutation throughout the passaging series (Fig. 3e and Extended Data Fig. 4d).

We recombinantly expressed and purified NSP14 single-mutant proteins (V290A, N306K, P335S, P335H, H424R and S503T; Extended Data Fig. 5a) and monitored their binding to SAH and/or TDI-015051 by thermal shift assay (Extended Data Fig. 5b). Wild-type NSP14 bound SAH with a ΔT_m of 4.3 °C, whereas most mutants showed reduced ΔT_m values. The P335S and P335H mutations affected SAH binding the most, with ΔT_m values of 0 °C and 0.7 °C, respectively. The ΔT_m values of the ternary complex with SAH and TDI-015051 dropped by 11.3 °C and 15.4 °C for P335S and P335H mutants, respectively, compared with wild type. The S503T mutation did not affect SAH binding and ternary complex formation and was therefore excluded from follow-up studies as it was probably selected due to cell culture adaptation and not compound resistance.

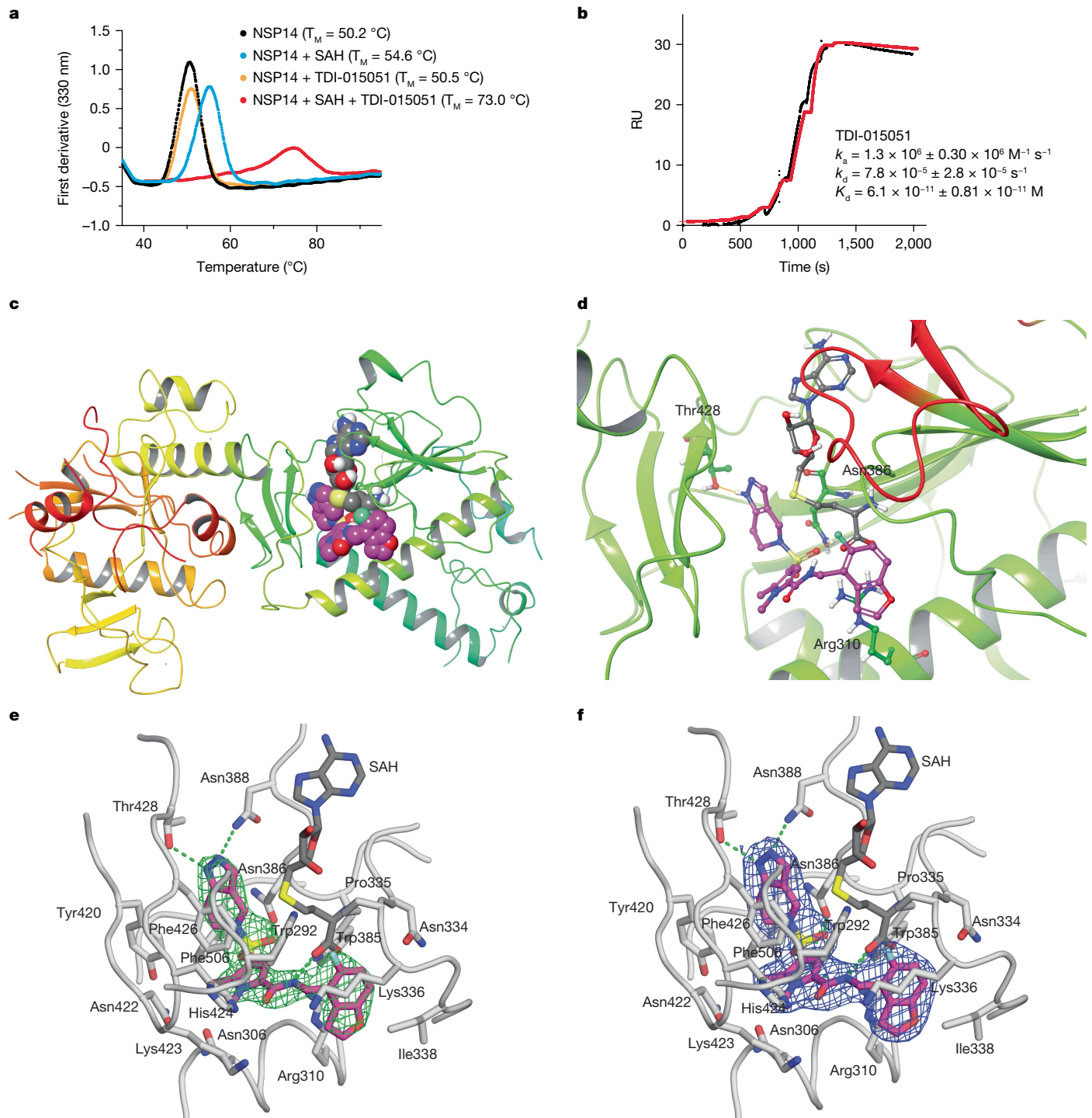


Fig. 2 | Biochemical and structural characterization of the NSP14–SAH–TDI-015051 inhibitory ternary complex. **a**, Thermal melting profiles in the first derivative mode of NSP14 (1 μM) alone or in the presence of SAH (25 μM) and/or TDI-015051 (20 μM) recorded at 330 nm over a temperature range of 35–95 °C. The T_m corresponds to the inflection point and is visualized as the peak of the curve. Profiles are representative of three independent experiments. **b**, Single-cycle kinetics surface plasmon resonance analysis revealing the binding of TDI-015051 (0–1 μM) to immobilized NSP14 in the presence of 10 μM SAH. RU, relative resonance units. The red line depicts a global fit of the response data (black line) to a 1:1 interaction model. **c**, Crystal structure of TDI-015051 in complex with SARS-CoV-2 NSP14 and SAH (Protein Data Bank (PDB) ID 8R7B). NSP14 is displayed as cartoon ribbons, with the exonuclease domain coloured red to yellow and the MTase domain coloured green to blue. SAH and TDI-015051 are displayed in space filling with grey and magenta carbon atoms.

Water molecules and heteroatomic species such as buffer ions or solvents are not shown. **d**, Binding site of TDI-015051 in complex with SARS-CoV-2 NSP14 and SAH. NSP14 is displayed as cartoon ribbons and green wires. Key residues are labelled and displayed in atom-coloured balls and sticks with green carbon atoms. SAH and TDI-015051 are displayed in atom-coloured balls and sticks with grey and magenta carbon atoms, respectively. Hydrogen bonding interactions between the ligand and the protein are indicated with dashed orange lines. The loop from Asp352 to Phe377 is displayed as a red cartoon ribbon. **e**, Fo–Fc electron density map of bound TDI-015051 contoured at the 4.0 σ level. The ligands and neighbouring protein side chains are shown as a stick model, coloured according to the chemical atom type ($C_{\text{TDI-015051}}$ in cyan, C_{SAH} in dark grey, C_{NSP14} in light grey, N in blue, O in red, S in yellow and F in pale cyan). Hydrogen bonds are indicated as green dashed lines. **f**, Refined 2Fo–Fc electron density map of bound TDI-015051 contoured at the 1.0 σ level.

Article

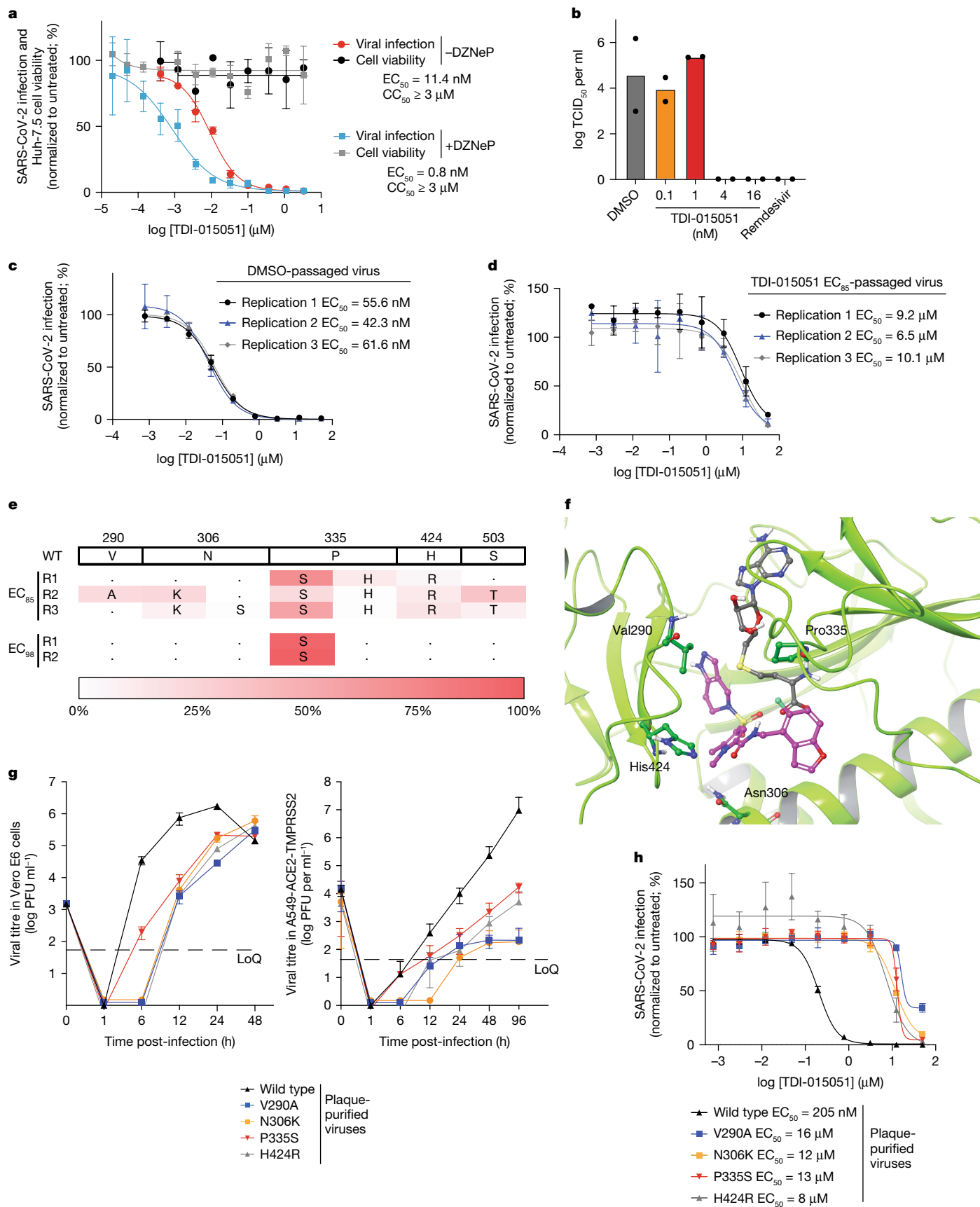


Fig. 3 | See next page for caption.

To address the effect of NSP14 mutations on viral replication, we obtained plaque-purified wild-type, NSP14(V290A), NSP14(N306K), NSP14(P335S) and NSP14(H424R) variant SARS-CoV-2 viruses.

Compared with wild-type virus, all variants showed impaired replication kinetics in Vero E6 and A549-ACE2-TMPRSS2 cells (Fig. 3g). We further compared the viral fitness between wild-type and NSP14(P335S)

Fig. 3 | Assessment of SARS-CoV-2 resistance mutation development to TDI-015051 in Vero E6 cells. **a**, SARS-CoV-2 antiviral activity and cytotoxicity of TDI-015051 in Huh-7.5 cells with or without co-treatment of 5 μM DZNeP. $n = 3$. Data are shown as mean ± s.d. **CC₅₀**, half-maximal cytotoxic concentration. **b**, Inhibition of SARS-CoV-2 viral replication in primary small airway human cells by TDI-015051 (0.1 nM, 1 nM, 4 nM or 16 nM). Treatment of cells with remdesivir (100 nM) served as a positive control for inhibition of SARS-CoV-2 replication; DMSO treatment served as a negative control. Viral titres were determined for the TCID₅₀ assay 4 days post-infection. $n = 2$ independent experiments. **c**, Inhibition of SARS-CoV-2 DMSO lineages (three replicates) after five passages by TDI-015051 in Vero E6 cells. $n = 3$. Data are shown as mean ± s.d. **d**, Inhibition of TDI-015051 EC₈₅-passaged SARS-CoV-2 (three replicates) after five passages by TDI-015051 in Vero E6 cells. $n = 3$. Data are shown as mean ± s.d. **e**, Amino acid

changes in NSP14 emerging after five passages of SARS-CoV-2 in Vero E6 cells in the presence of TDI-015051 (EC₈₅ or EC₉₉). Changes are shaded according to frequency (in %). R1, replication 1; WT, wild type. **f**, Binding site of TDI-015051 in complex with SARS-CoV-2 NSP14 and SAH. The protein is displayed as cartoon ribbons. Residues Val290, Asn306, Pro335 and His424 are labelled and displayed in atom-coloured balls and sticks with green carbon atoms. SAH and TDI-015051 are displayed in atom-coloured balls and sticks with grey and magenta carbon atoms, respectively. **g**, Replication of wild-type and NSP14-mutant plaque-purified SARS-CoV-2 viruses in Vero E6 (left) or A549-ACE2-TMPRSS2 (right) cells, respectively. The numbers of viral infectious particles are graphed as log₁₀ PFU ml⁻¹. $n = 5$. Data are shown as mean ± s.d. LoQ, limit of quantification. **h**, TDI-015051-mediated inhibition of infection of plaque-purified SARS-CoV-2 in Vero E6 cells. $n = 5$. Data are shown as mean ± s.d.

plaque-purified viruses in co-culture starting at a 1:9 ratio (Extended Data Fig. 5c). After one passage, more than 89% of the viral population encoded wild-type P335, and further increased to more than 99% after two passages, indicating that the NSP14(P335S) variant was at a competitive disadvantage relative to wild type.

NSP14(V290A), NSP14(N306K), NSP14(P335S) and NSP14(H424R) plaque-purified viruses showed resistance to TDI-015051 and their respective EC₅₀ values were elevated 40-fold or more relative to wild type (Fig. 3h). To exclude that additional SARS-CoV-2 mutations outside of NSP14 contributed to the TDI-015051 resistance, we generated infectious clone-derived wild-type and NSP14(V290A), NSP14(N306K), NSP14(P335S) and NSP14(H424R) mutant viruses, which were sequence verified across the entire genome. Although infectious clone-derived wild-type virus was sensitive to TDI-015051 (EC₅₀ = 61 nM), all mutant viruses showed resistance with 40–250-fold elevated EC₅₀ values (Extended Data Fig. 5d). Inhibition of replication of infectious clone-derived wild-type and NSP14-mutant viruses by nirmatrelvir⁶, the FDA-approved orally active SARS-CoV-2 3CL protease inhibitor, remained unimpaired (Extended Data Fig. 5e). These results indicate that various NSP14 mutational strategies of SARS-CoV-2 confer resistance to TDI-015051, albeit by compromising viral fitness.

To evaluate potential synergy between TDI-015051 and nirmatrelvir, we co-dosed both compounds in Huh-7.5 cells and evaluated their effect on SARS-CoV-2 viral replication. We analysed the generated dose-response matrix using the Loewe model and the SynergyFinder tool²⁷ and obtained an average Loewe synergy score of 26.4 and the most synergistic area score of 40.3 (Extended Data Fig. 5f), suggesting that the combination of TDI-015051 and nirmatrelvir is likely to be synergistic.

TDI-015051 inhibits NSP14 of other hCoVs

TDI-015051 inhibited NSP14 of coronaviruses from different genera of the *Coronaviridae* family. NSP14 of the alphacoronaviruses α-hCoV-NL63 and α-hCoV-229E, as well as the betacoronavirus β-hCoV-MERS, which share more than 50% amino acid sequence identity with SARS-CoV-2 NSP14, were inhibited with apparent IC₅₀ values of 1.7 nM, 2.6 nM or 3.6 nM, respectively, in our biochemical assay (Extended Data Fig. 6a). However, because these values mirror the enzyme concentration used in the biochemical assays (Supplementary Table 1), they are probably an underestimate of the true biochemical potency.

In the presence of SAH, TDI-015051 increased the T_M of hCoV-NL63, hCoV-229E or MERS NSP14 by 20 °C, 14.2 °C or 17.1 °C, respectively (Extended Data Fig. 6b–d). TDI-015051 inhibited hCoV-NL63 and hCoV-229E infection in Huh-7.5 cells with EC₅₀ of 0.12 μM and 3.7 μM, respectively (Extended Data Fig. 6e,f), as well as β-hCoV-MERS infection in A549-ACE2-DPP4-TMPRSS2 cells with an EC₅₀ of 6.5 μM (Extended Data Fig. 6g).

To evaluate the selectivity of TDI-015051, we expressed and purified the SARS-CoV-2 NSP16-NSP10 2'-O-cap MTase complex from *Escherichia coli*. We confirmed that m⁷GpppA(N)₉, representing the first ten

nucleotides of the leader sequence of the SARS-CoV-2 genome, but not unmethylated GpppA(N)₉, was 2'-O-methylated by NSP16-NSP10 (ref. 28) (Extended Data Fig. 6h), and then showed that addition of TDI-015051 did not interfere with 2'-O-methylation (Extended Data Fig. 6i). Furthermore, addition of TDI-015051 did not inhibit the human RNA guanine-7 methyltransferase (RNMT) in complex with its protein cofactor RAM²⁹ (Extended Data Fig. 6j) nor NS5 MTase from Zika virus^{30,31} (Extended Data Fig. 6k). SARS-CoV-2 NSP14, ZIKV NS5 and human RNMT have distinct protein folds and share less than 20% sequence identity.

TDI-015051 inhibits viral translation

N7 methylation of the mRNA cap ensures efficient recognition by eukaryotic translation initiation factors and translation of host and viral mRNAs^{9–11,32}. To evaluate the effect of TDI-015051 on mRNA translation, we pre-treated Vero E6 cells with DMSO, EC₅₀ or EC₉₉ concentrations of TDI-015051 and then infected the cell culture for 8 h with SARS-CoV-2. Polysome profiles of mock-infected and virus-infected cell lysates were comparable and unaffected by the presence of TDI-015051 (Extended Data Fig. 7a). To evaluate whether TDI-015051 selectively affected viral mRNA translation, we first determined the relative abundance of SARS-CoV-2 nucleocapsid mRNA relative to host HPRT1 mRNA by quantitative PCR with reverse transcription (RT-qPCR) in mock-treated or TDI-015051-treated SARS-CoV-2-infected Vero E6 cells. Treatment of cells with an EC₉₉ concentration of TDI-015051 caused a 2,200-fold reduction of viral RNA levels compared with mock treatment (Extended Data Fig. 7b, left panel). Furthermore, the residual viral mRNA distribution in the polysomal fraction compared with the ribosome-free fraction was reduced 35-fold (Extended Data Fig. 7b, right panel), indicating that TDI-015051 specifically impaired viral mRNA translation and also downstream replication.

To evaluate whether TDI-015051 affected SARS-CoV-2 evasion from innate immunity, we infected A549-ACE2-TMPRSS2 cells with SARS-CoV-2 and measured relative mRNA levels of interferon-stimulated genes by RT-qPCR. The presence of TDI-015051 at EC₉₅ caused a small induction of interferon-stimulated genes compared with DMSO-treated or nirmatrelvir-treated cells (Extended Data Fig. 7c), suggesting that residual unmethylated viral RNA induced a weak type I interferon-mediated immune response³³.

In vivo antiviral efficacy of TDI-015051

TDI-015051 showed good solubility in PBS (0.8 μM) and high permeability (PAMPA; 18×10^{-6} cm s⁻¹). TDI-015051 demonstrated moderate-to-low stability in human, rat, mouse and dog liver microsomes (44, 99, 85 and 26 μl min⁻¹ mg⁻¹, respectively; Extended Data Fig. 7d). TDI-015051 was a potent inhibitor of CYP3A4 (IC₅₀ = 0.02 μM). Potent CYP inhibitors are associated with drug–drug interactions and restrict co-administered medications. Yet, potent CYP inhibitors, such as ritonavir, are FDA approved in combination with antivirals to safely boost oral exposure

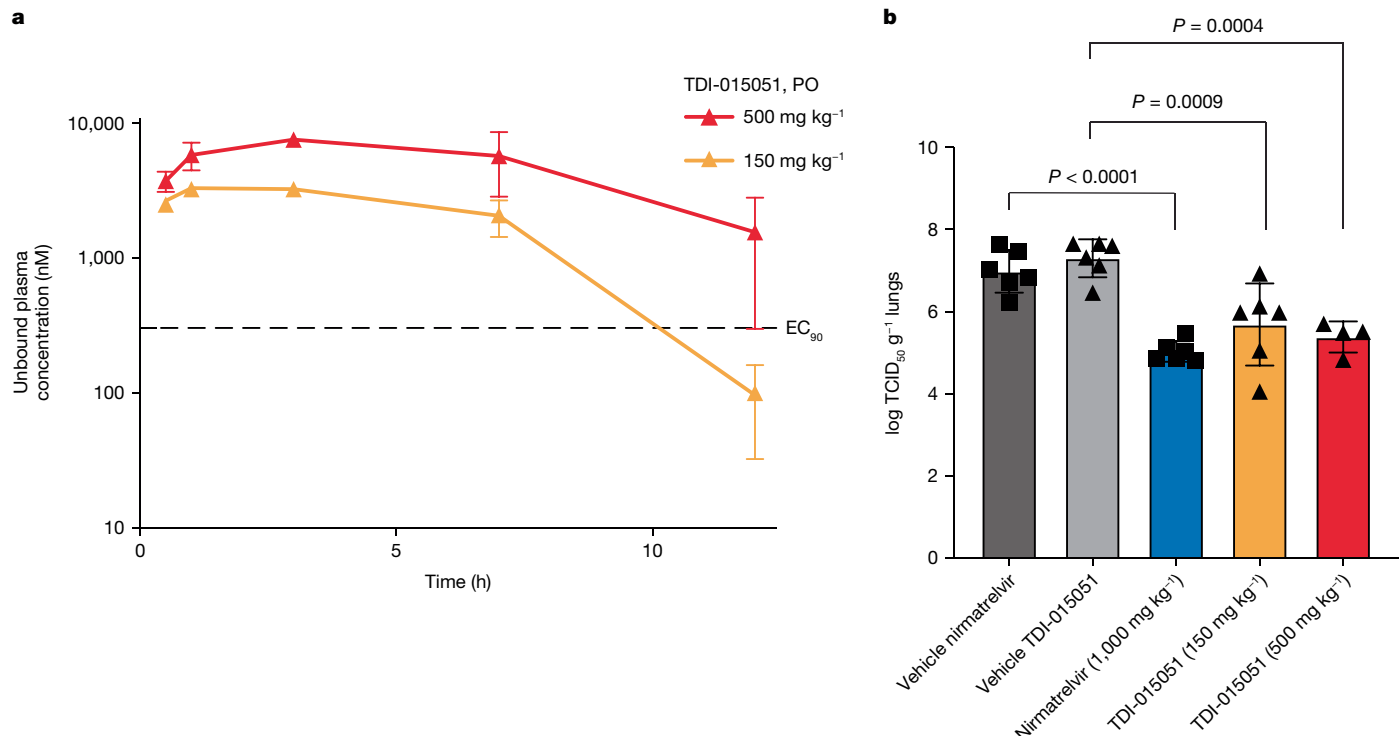


Fig. 4 | Antiviral efficacy of TDI-015051 in a K18-hACE2 transgenic mouse model of SARS-CoV-2 infection. **a**, Twelve-hour TDI-015051 exposure levels of 150 mg kg⁻¹ or 500 mg kg⁻¹ doses in uninfected, orally dosed CD-1 mice ($n = 3$; data are shown as mean \pm s.d.) using a PEG400-based solution formulation. The EC₉₀ of 300 nM, determined in a Vero E6 cell-based antiviral assay (Extended

Data Fig. 4a), is shown as a dashed line. PO, oral gavage. **b**, Viral lung titres of mice in all study groups were determined at day 4 post-infection. Lung titres are graphed as log₁₀ TCID₅₀ g⁻¹ lungs. Adjusted P values by ordinary one-way analysis of variance are given. From left to right on the x axis, $n = 6$ for groups 1–4 and $n = 4$ for group 5. Data are shown as mean \pm s.d.

and efficacy^{6,34,35}. Initial pharmacokinetic screening for TDI-015051 was performed by intravenous dosing at 5 mg kg⁻¹ and by oral gavage at doses of 10 mg kg⁻¹ and 50 mg kg⁻¹. The intravenous pharmacokinetic screening of TDI-015051 demonstrated a short half-life and high clearance. TDI-015051 exhibited significant non-linear oral pharmacokinetics. Increasing the oral dose from 10 mg kg⁻¹ to 50 mg kg⁻¹ resulted in a tenfold increase in the respective dose-corrected area under the curve. The non-linear increase in exposure was attributed to the potent CYP3A4 inhibition. The subsequent single-dose oral gavage pharmacokinetics study was performed at 150 mg kg⁻¹ and 500 mg kg⁻¹ over a 12-h interval to profile the first dose of a twice daily dosing regimen. The free fraction of TDI-015051 in plasma was above the Vero E6 cell EC₉₀ of 300 nM for the entire 12-h interval at 500 mg kg⁻¹ and for approximately 10 h at 150 mg kg⁻¹ (Fig. 4a).

We next evaluated the *in vivo* efficacy of orally administered TDI-015051 to reduce SARS-CoV-2 viral lung burden in a K18-hACE2 transgenic mouse model^{36,37} compared with nirmatrelvir⁶. Two studies were conducted: dosing inhibitor and vehicle controls either 12 h post-infection (Fig. 4b and Extended Data Fig. 8a–d) or 1 h before infection (Extended Data Fig. 8e–i), respectively, followed by dosing twice daily from day 0 to day 3 post-infection. The more stringent post-infection study showed no substantial weight loss across the 4-day treatment for control or inhibitor treatments (Extended Data Fig. 8b). However, the lung viral titres, as determined by TCID₅₀ assays, showed robust infection in the lungs of control-treated mice and similar, approximately 2 orders of magnitude, reduction of viral titres for nirmatrelvir-treated or TDI-015051-treated mice (Fig. 4b). These results were independently confirmed by performing PFU assays or RT-qPCR analyses of the SARS-CoV-2 E mRNA using lung tissue lysates (Extended Data Fig. 8c,d). The prophylactic dose studies showed an order of magnitude higher repression of viral titres than post-infection dosing and, again, similar effects for both nirmatrelvir and TDI-015051 (Extended Data Fig. 8e–i).

In summary, we have identified uncharged, noncovalent inhibitors of coronavirus NSP14 MTase with picomolar affinity and slow dissociation kinetics that bind to the viral cap-binding pocket in the presence of SAH, forming a ternary inhibitory complex. Unlike inhibitors based on displacement of the universal SAM–enzyme–cofactor or SAH–enzyme–cofactor, new drugs, which displace the MTase-specific unique substrate of methylation, promise to be highly selective. This new class of inhibitors may complement existing SARS-CoV-2 antivirals and could minimize the development of viral resistance in combination therapy. Finally, structurally distinct mRNA cap MTases are encoded by other viruses of pandemic concern, including DNA viruses replicating in the cytosol, illuminating new avenues for antiviral drug discovery.

Online content

Any methods, additional references, Nature Portfolio reporting summaries, source data, extended data, supplementary information, acknowledgements, peer review information; details of author contributions and competing interests; and statements of data and code availability are available at <https://doi.org/10.1038/s41586-024-08320-0>.

- Phillips, N. The coronavirus is here to stay — here's what that means. *Nature* **590**, 382–384 (2021).
- Dolgin, E. Pan-coronavirus vaccine pipeline takes form. *Nat. Rev. Drug Discov.* **21**, 324–326 (2022).
- Chaudhary, N., Weissman, D. & Whitehead, K. A. mRNA vaccines for infectious diseases: principles, delivery and clinical translation. *Nat. Rev. Drug Discov.* **20**, 817–838 (2021).
- Li, G., Hilgenfeld, R., Whitley, R. & Clercq, E. D. Therapeutic strategies for COVID-19: progress and lessons learned. *Nat. Rev. Drug Discov.* **22**, 449–475 (2023).
- Malone, B., Urakova, N., Snijder, E. J. & Campbell, E. A. Structures and functions of coronavirus replication-transcription complexes and their relevance for SARS-CoV-2 drug design. *Nat. Rev. Mol. Cell Biol.* **23**, 21–39 (2022).
- Owen, D. R. et al. An oral SARS-CoV-2 M pro inhibitor clinical candidate for the treatment of COVID-19. *Science* **374**, 1586–1593 (2021).
- Nencka, R. et al. Coronaviral RNA-methyltransferases: function, structure and inhibition. *Nucleic Acids Res.* **50**, 635–650 (2022).

8. Decroly, E., Ferron, F., Lescar, J. & Canard, B. Conventional and unconventional mechanisms for capping viral mRNA. *Nat. Rev. Microbiol.* **10**, 51–65 (2011).
9. Both, G. W., Furuchi, Y., Muthukrishnan, S. & Shatkin, A. J. Ribosome binding to reovirus mRNA in protein synthesis requires 5' terminal 7-methylguanosine. *Cell* **6**, 185–195 (1975).
10. Muthukrishnan, S., Both, G. W., Furuchi, Y. & Shatkin, A. J. 5'-Terminal 7-methylguanosine in eukaryotic mRNA is required for translation. *Nature* **255**, 33–37 (1975).
11. Both, G. W., Banerjee, A. K. & Shatkin, A. J. Methylation-dependent translation of viral messenger RNAs in vitro. *Proc. Natl Acad. Sci. USA* **72**, 1189–1193 (1975).
12. Ferron, F., Decroly, E., Selisko, B. & Canard, B. The viral RNA capping machinery as a target for antiviral drugs. *Antivir. Res.* **96**, 21–31 (2012).
13. Zhang, J. & Zheng, Y. G. SAM/SAH analogs as versatile tools for SAM-dependent methyltransferases. *ACS Chem. Biol.* **11**, 583–597 (2016).
14. Czarna, A. et al. Refolding of lid subdomain of SARS-CoV-2 nsp14 upon nsp10 interaction releases exonuclease activity. *Structure* **30**, 1050–1054.e2 (2022).
15. Ma, Y. et al. Structural basis and functional analysis of the SARS coronavirus nsp14–nsp10 complex. *Proc. Natl Acad. Sci. USA* **112**, 9436–9441 (2015).
16. Ferron, F. et al. Structural and molecular basis of mismatch correction and ribavirin excision from coronavirus RNA. *Proc. Natl Acad. Sci. USA* **115**, E162–E171 (2018).
17. Imprachim, N., Yosaatmadja, Y. & Newman, J. A. Crystal structures and fragment screening of SARS-CoV-2 NSP14 reveal details of exoribonuclease activation and mRNA capping and provide starting points for antiviral drug development. *Nucleic Acids Res.* **51**, 475–487 (2022).
18. Kottur, J., Rechkoblit, O., Quintana-Feliciano, R., Sciaky, D. & Aggarwal, A. K. High-resolution structures of the SARS-CoV-2 N7-methyltransferase inform therapeutic development. *Nat. Struct. Mol. Biol.* **29**, 850–853 (2022).
19. Liu, C. et al. Structural basis of mismatch recognition by a SARS-CoV-2 proofreading enzyme. *Science* **373**, 1142–1146 (2021).
20. Bootsma, A. N. & Wheeler, S. E. Tuning stacking interactions between Asp–Arg salt bridges and heterocyclic drug fragments. *J. Chem. Inf. Model.* **59**, 149–158 (2019).
21. Craft, M. K. & Waldrop, G. L. Mechanism of biotin carboxylase inhibition by ethyl 4-[[2-chloro-5-(phenylcarbamoyl)phenyl]sulphonylamino]benzoate. *J. Enzyme Inhib. Med. Chem.* **37**, 100–108 (2022).
22. Ward, W. H. J. et al. Kinetic and structural characteristics of the inhibition of enoyl (acyl carrier protein) reductase by triclosan. *Biochemistry* **38**, 12514–12525 (1999).
23. Vizán, P., Croce, L. D. & Aranda, S. Functional and pathological roles of AHCY. *Front. Cell Dev. Biol.* **9**, 654344 (2021).
24. Chiang, P. K. & Cantoni, G. L. Perturbation of biochemical transmethylations by 3-deazaadenosine in vivo. *Biochem. Pharmacol.* **28**, 1897–1902 (1979).
25. Wang, L. et al. Susceptibility to SARS-CoV-2 of cell lines and substrates commonly used to diagnose and isolate influenza and other viruses. *Emerg. Infect. Dis.* **27**, 1380–1392 (2021).
26. Ogando, N. S. et al. Structure–function analysis of the nsp14 N7-guanine methyltransferase reveals an essential role in Betacoronavirus replication. *Proc. Natl Acad. Sci. USA* **118**, e2108709118 (2021).
27. Janevski, A., Giri, A. K. & Aittokallio, T. SynergyFinder 3.0: an interactive analysis and consensus interpretation of multi-drug synergies across multiple samples. *Nucleic Acids Res.* **50**, W739–W743 (2022).
28. Park, G. J. et al. The mechanism of RNA capping by SARS-CoV-2. *Nature* **609**, 793–800 (2022).
29. Varshney, D. et al. Molecular basis of RNA guanine-7 methyltransferase (RNMT) activation by RAM. *Nucleic Acids Res.* **44**, 10423–10436 (2016).
30. Zhao, B. et al. Structure and function of the Zika virus full-length NS5 protein. *Nat. Commun.* **8**, 14762 (2017).
31. Coutard, B. et al. Zika virus methyltransferase: structure and functions for drug design perspectives. *J. Virol.* **91**, e02202–16 (2017).
32. Filipowicz, W. et al. A protein binding the methylated 5'-terminal sequence, m7GpppN, of eukaryotic messenger RNA. *Proc. Natl Acad. Sci. USA* **73**, 1559–1563 (1976).
33. Pan, R. et al. N7-methylation of the coronavirus RNA cap is required for maximal virulence by preventing innate immune recognition. *mBio* **13**, e03662–21 (2022).
34. Cvetkovic, R. S. & Goa, K. L. Lopinavir/ritonavir: a review of its use in the management of HIV infection. *Drugs* **63**, 769–802 (2003).
35. McKeage, K., Perry, C. M. & Kearns, S. J. Darunavir: a review of its use in the management of HIV infection in adults. *Drugs* **69**, 477–503 (2009).
36. McCray, P. B. et al. Lethal infection of K18-hACE2 mice infected with severe acute respiratory syndrome coronavirus. *J. Virol.* **81**, 813–821 (2007).
37. Winkler, E. S. et al. SARS-CoV-2 infection of human ACE2-transgenic mice causes severe lung inflammation and impaired function. *Nat. Immunol.* **21**, 1327–1335 (2020).

Publisher's note Springer Nature remains neutral with regard to jurisdictional claims in published maps and institutional affiliations.

Springer Nature or its licensor (e.g. a society or other partner) holds exclusive rights to this article under a publishing agreement with the author(s) or other rightsholder(s); author self-archiving of the accepted manuscript version of this article is solely governed by the terms of such publishing agreement and applicable law.

© The Author(s), under exclusive licence to Springer Nature Limited 2024

Article

Reporting summary

Further information on research design is available in the Nature Portfolio Reporting Summary linked to this article.

Data availability

RNA sequencing data generated during the study are available on the NCBI Sequence Read Archive (SRA) under the BioProject number PRJNA1035531. High-throughput screening data, structures of compounds, SMILES chemical notations and NPI data are downloadable in the Open Science Framework (https://osf.io/xk5uf/?view_only=01b3077a87cd495fb21e51e0dba4cf9f). X-ray crystallographic coordinates and structure factor files have been deposited at the RCSB Protein Data Bank under accession number 8R7B. Source data are provided with this paper.

Acknowledgements We thank B. ten’Oever for providing total RNA from SARS-CoV-2-infected cells at the onset of the pandemic; K. Huynh for cloning and purification of the hRNMT-RAM complex under supervision of A.G.; members of the Tuschl laboratory for their support and critical review of the manuscript; W. Xie and D.J. Patel for large-scale purification of NSP14 from cell pellets provided by C.M. for high-throughput screening (HTS) and hit validation; A. Stern (CEPTER Biopartners) for large-scale expression and purification of SARS-CoV-2 NSP14 during the medchem phase of the program, as well as protein purification of MERS-CoV NSP14; M. B. Murphy for helpful discussions on the analysis of surface plasmon resonance data; and C. Mendez-Romero, T. Tillery, A. Rojas-Triana and D. Villalba-Guzman of the CDI Animal Model Core for their contribution to the technical execution of the *in vivo* animal proof-of-concept study. This research was funded by the NIH/NIAID (IU19AI171401, Metropolitan Antiviral Drug Accelerator (MAVDA)), the Rockefeller University Robertson Therapeutic Development Funds (to C.M. and T.T.) and a grant from the JPB Foundation to Rockefeller University. This research was supported by the Stavros Niarchos Foundation (SNF) as part of its grant to the SNF Institute for Global Infectious Disease Research at The Rockefeller University. The RU Proteomics Resource Center acknowledges funding from The Leona M. and Harry B. Helmsley Charitable Trust for mass spectrometer instrumentation. We acknowledge the support of the F. M. Kirby Foundation for funding the purchase of the Biotek Synergy NEO instrument used in this study; and the Sanders Tri-Institutional Therapeutics Discovery Institute (TDI), a 501(c)(3) organization. TDI and Proteros Biostructures acknowledge financial support from Takeda Pharmaceutical

Company. TDI also receives financial support from TDI’s parent institutes (Memorial Sloan Kettering Cancer Center, The Rockefeller University and Weill Cornell Medicine) and from a contribution from L. Sanders and other philanthropic sources.

Author contributions C.M., A.G. and T.T. initiated the project. C.M. and A.G. constructed expression vectors, established recombinant protein purification protocols and purified recombinant proteins. C.M., L.R.-E., M.-R.M. and C.L. developed the NSP14 HTS assay. C.M. performed the HTS and hit-validation experiments. C.M. designed, executed and interpreted the biochemical and biophysical assays for inhibitor characterization with support from J.A.D. H.-H.H. performed the biosafety level 3 (BSL3) work for cell-based viral infection assays, including production of SARS-CoV-2 stocks and viral infections. A.W.A. and S.Y.J. performed the BSL3 work for all viral resistance studies, including the generation of plaque-purified and infectious clone-derived wild-type and mutant SARS-CoV-2 viruses. A.G. analysed the RNA sequencing data to identify SARS-CoV-2 resistance mutations to TDI-015051. M.W.M. was the lead medicinal chemist. D.J.H. was the lead computational chemist. M.W.M., D.J.H. and N.L. were responsible for the design and preparation of the compounds based on the RU-0415529 scaffold. C.M. performed the cell culture work for determination of intracellular SAH or SAM concentrations. H.A. performed the mass spectrometric analyses and quantification with oversight by H.M. J.N., O.G. and S.S. solved the co-crystal structures. M.Z. optimized the compound formulation and performed compound dosing and pharmacokinetics in mice with the support of J.C. (pharmacokinetic dosing) and S.P.-L. (high-performance liquid chromatography–mass spectrometry sample analyses). A.M.N. and V.S. designed the antiviral efficacy studies of TDI-015051 in a K18-hACE2 transgenic mouse model of SARS-CoV-2 infection, which were executed with support from E.D. V.S. performed the *ex vivo* assays (TCID₅₀, PFU and RT-qPCR) and analyses. A.M.N. and V.S. interpreted all corresponding *in vivo* and *ex vivo* data. The air–liquid interface experiment was designed by N.A. and C.M., and executed by I.G. and N.A. with support from R.R. and K.G. C.-W.C. performed the MERS-CoV inhibition study with support from N.O. J.F.G. designed, curated and annotated the compound library. R.W.M. and S.K. helped coordinate the project and consulted on assay development and data interpretation. J.F.G., D.S.P., P.T.M., C.M.R. and T.T. provided general project oversight and coordination of their research teams. C.M., A.G. and T.T. wrote the manuscript with input from all authors.

Competing interests The authors declare no competing interests. The Rockefeller University filed patent application PCT/US2024/012695 titled ‘Sulfonamide-1H-pyrrole-2-carboxamide inhibitors of SARS-CoV-2 NSP14 methyltransferase and derivatives thereof’.

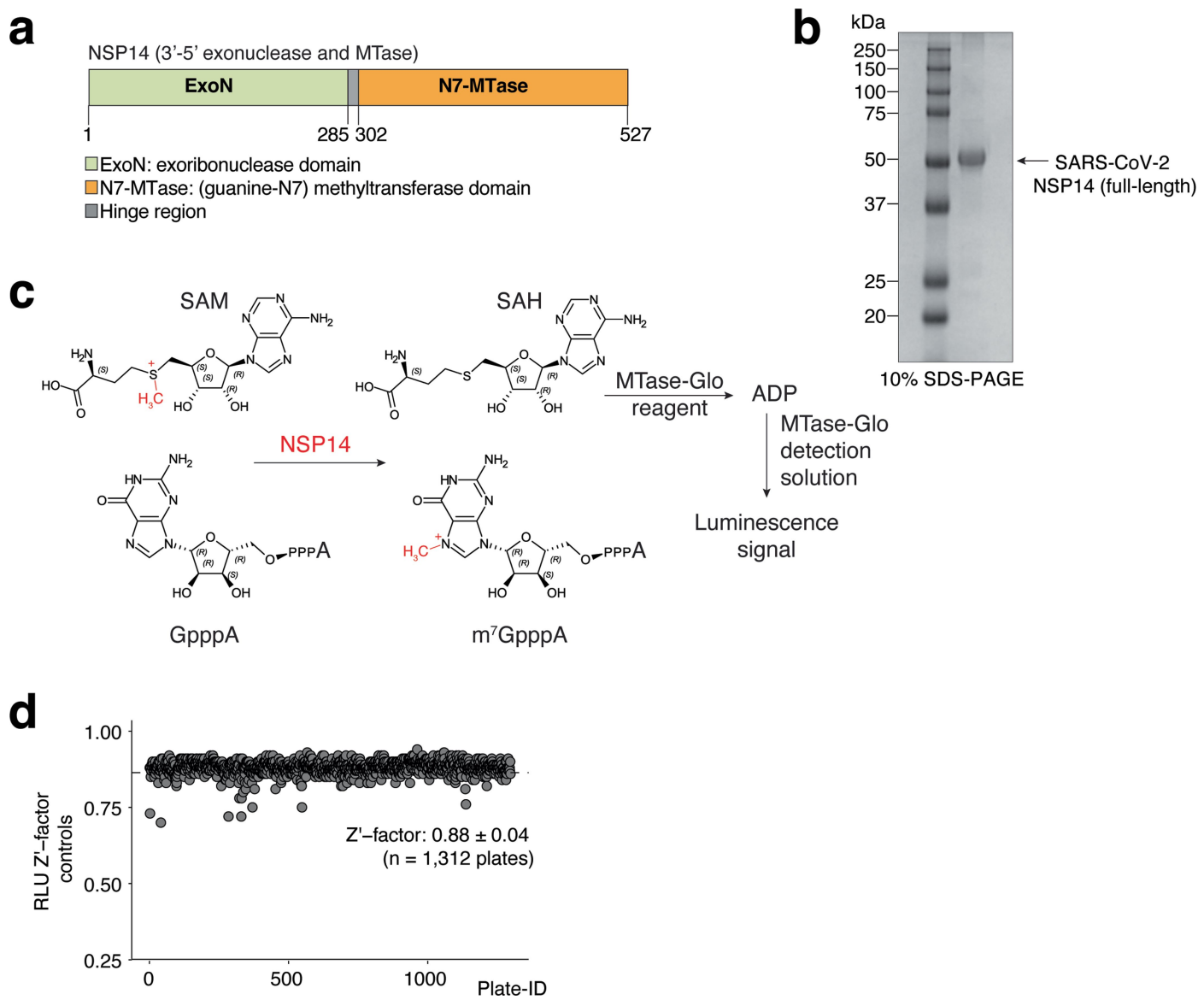
Additional information

Supplementary information The online version contains supplementary material available at <https://doi.org/10.1038/s41586-024-08320-0>.

Correspondence and requests for materials should be addressed to Thomas Tuschl.

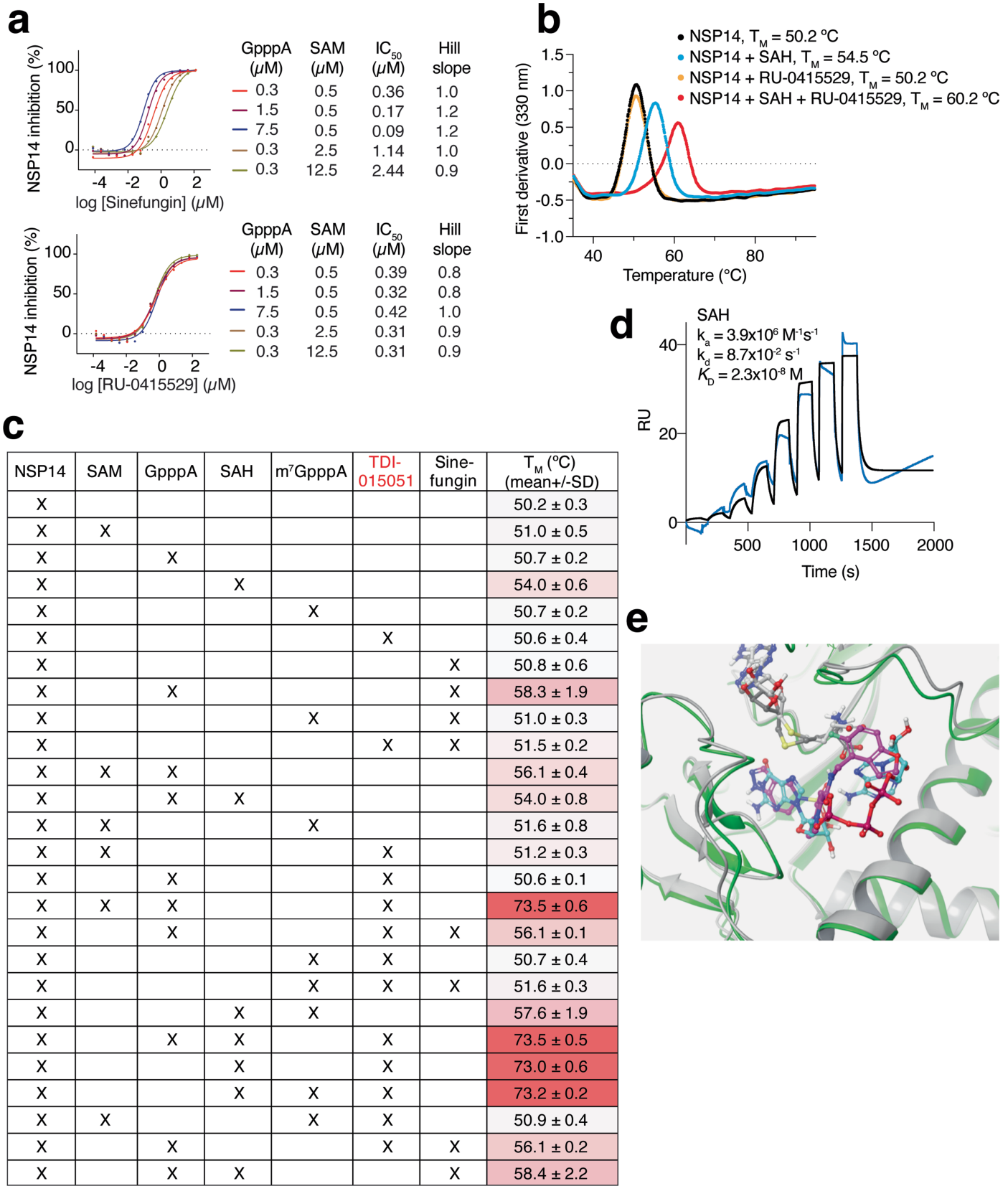
Peer review information *Nature* thanks Yunjeong Kim, Timothy Sheahan, Pei-Yong Shi and the other, anonymous, reviewer(s) for their contribution to the peer review of this work.

Reprints and permissions information is available at <http://www.nature.com/reprints>.



Extended Data Fig. 1 | Identification of RU-0415529 and development of TDI-01501. **a)** Domain organization of SARS-CoV-2 NSP14. **b)** Representative gel image of $n = 2$ biological replicates of SDS-PAGE analysis and Coomassie brilliant blue staining of purified full-length SARS-CoV-2 NSP14 protein (2 μ g loaded). For gel source data, see Supplementary Fig. 1. **c)** High-throughput biochemical screening assay for the identification of small-molecule SARS-CoV-2

Article

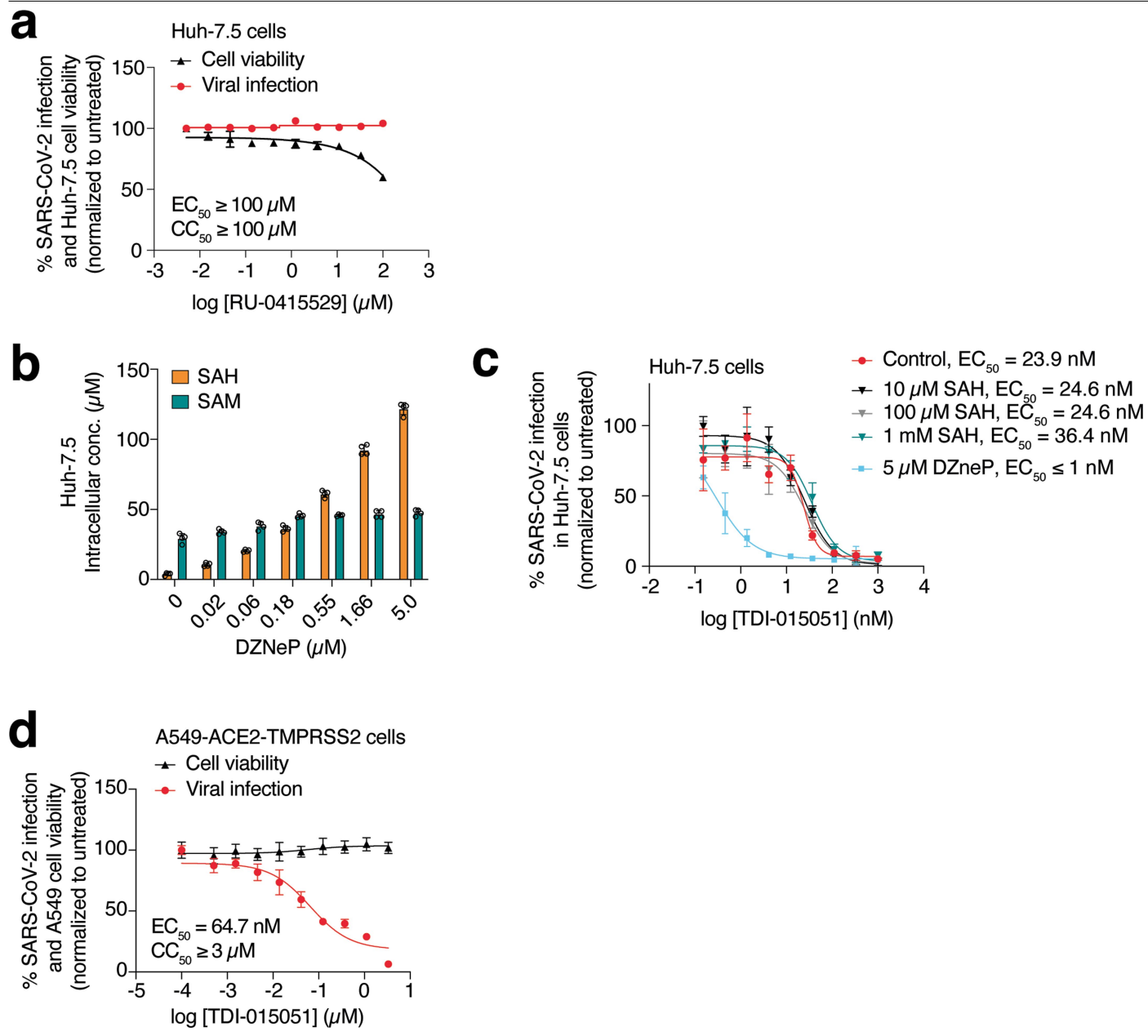


Extended Data Fig. 2 | See next page for caption.

Extended Data Fig. 2 | Characterization of the NSP14-SAHC-TDI-015051 inhibitory ternary complex. **a)** Inhibition of SARS-CoV-2 NSP14 by sinefungin and RU-0415529 at varying GpppA and SAM substrate concentrations using the luminescence-based MTase-GloTM Assay (Promega). Data are represented as mean values; n = 3. **b)** Unfolding profiles of NSP14 (1 μM) alone or in presence of SAHC (25 μM) and/or RU-0415529 (20 μM) recorded at 330 nm over a temperature range from 35 °C to 95 °C, displayed in the first derivative mode. The melting temperature (T_m) corresponds to the inflection point and is visualized as the peak of the 1st derivative curve. Profiles are representative of 3 independent experiments. **c)** NSP14 (1 μM) melting temperatures (T_m) in presence of individual binding partners (20 μM each) or combinations thereof (n = 3, mean ± SD).

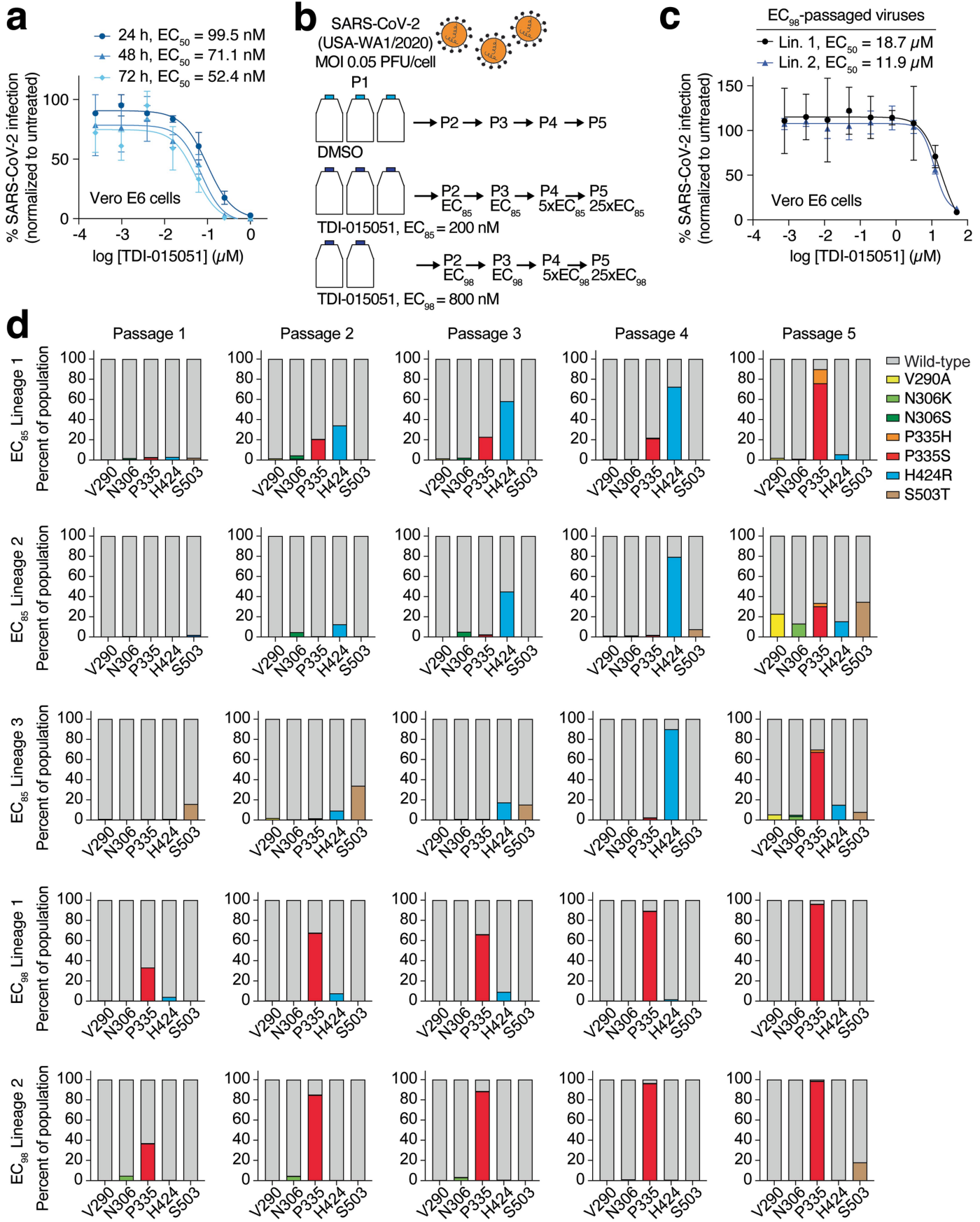
d) Single cycle kinetics SPR analysis revealing the binding of SAHC (0 - 1 μM) to immobilized NSP14. RU, relative resonance units. The blue line depicts a global fit of the response data (black line) to a 1:1 interaction model. **e)** Binding site of TDI-015051 in the complex with SARS-CoV-2 NSP14, SAHC, and GpppA. The coordinates for the SARS-CoV-2 and SARS-CoV-1 complexes correspond to PDB ID 8R7B and 5C8S¹⁵, respectively. The proteins are displayed as green and grey cartoon ribbons respectively. SAHC, TDI-015051, and GpppA are displayed in atom-colored balls and sticks with grey, magenta, and cyan carbon atoms, respectively. The exocyclic pyrazole group of TDI-015051 overlays the guanine ring of GpppA.

Article



Extended Data Fig. 3 | Cell-based anti-SARS-CoV-2 activity of RU-0415529 or TDI-015051. **a)** Anti-SARS-CoV-2 activity and cytotoxicity of RU-0415529 in Huh-7.5 cells. $n = 3$ biological replicates; mean \pm SD. **b)** Mass spectrometric quantification of intracellular levels of SAM and SAH in Huh-7.5 cells treated without or with DZNeP (0–5 μM) for 24 h. $n = 4$; mean \pm SD. **c)** Anti-SARS-CoV-2 activity of TDI-015051 in Huh-7.5 cells in absence or presence of 10 μM , 100 μM ,

or 1 mM SAH, respectively. Addition of the SAHase inhibitor DZNeP (5 μM) served as positive control to increase the cell-based activity of TDI-015051. $n = 3$ biological replicates; mean \pm SD. **d)** Anti-SARS-CoV-2 activity and cytotoxicity of TDI-015051 in A549-ACE2-TMPRSS2 cells. $n = 3$ biological replicates; mean \pm SD.

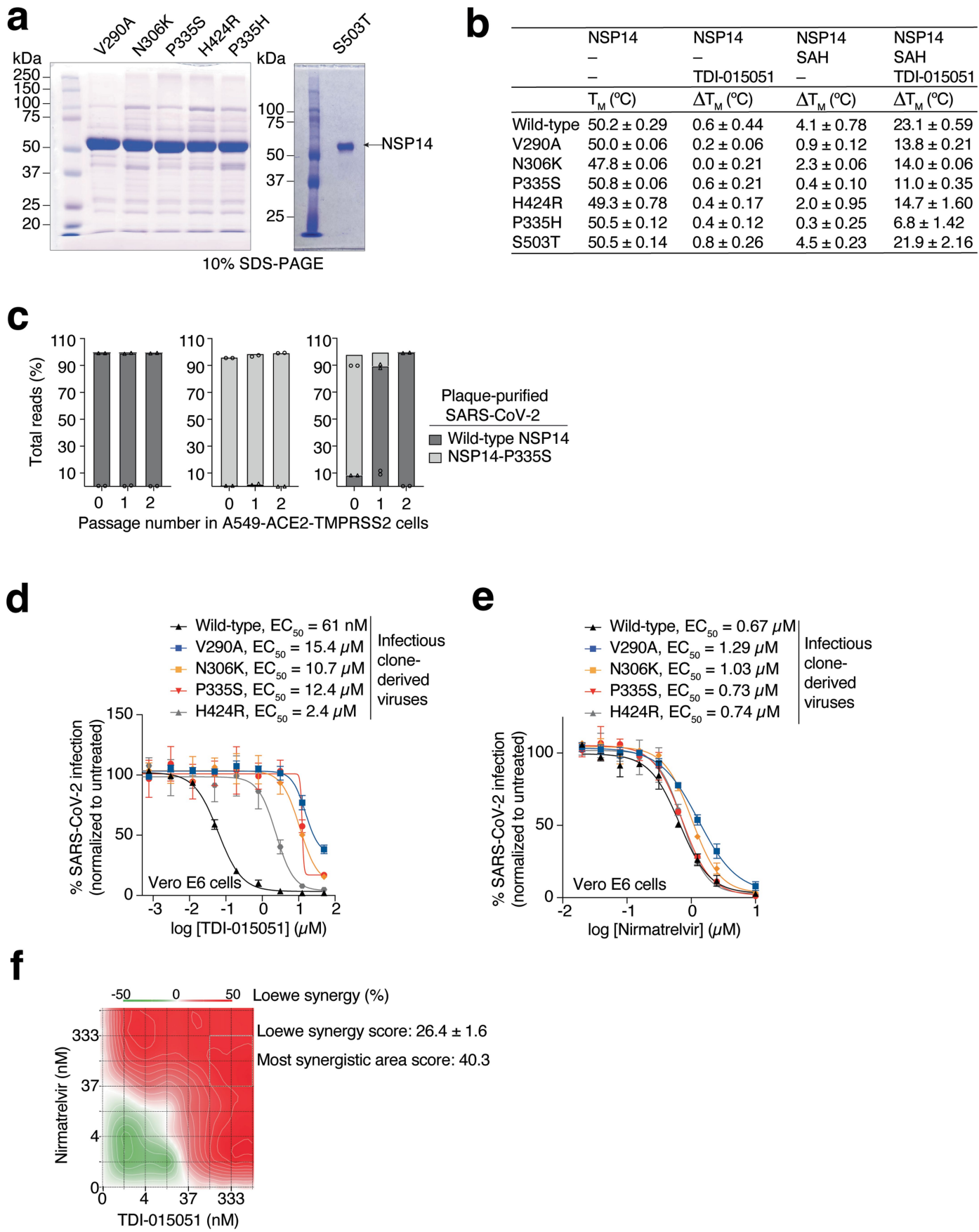


Extended Data Fig. 4 | See next page for caption.

Article

Extended Data Fig. 4 | Development of SARS-CoV-2 resistance mutations to TDI-015051 in Vero E6 cells. **a)** SARS-CoV-2 antiviral activity of TDI-015051 in Vero E6 cells. Cells were pre-incubated with compound for 1 h and then infected with SARS-CoV-2. After 24 h, 48 h, or 72 h of infection, cells were fixed and stained for SARS-CoV-2 nucleocapsid protein to determine viral infection. $n = 3$; mean \pm SD. **b)** SARS-CoV-2 passaging scheme to determine

resistance mutation development to TDI-015051 in Vero E6 cells. **c)** Inhibition of TDI-015051 EC₉₅-passaged viruses (2 replicates) after P5 by TDI-015051. $n = 3$; mean \pm SD. **d)** Percent of NSP14 amino acid changes emerging in 5 different SARS-CoV-2 lineages after each of 5 passages in Vero E6 cells challenged with TDI-015051.

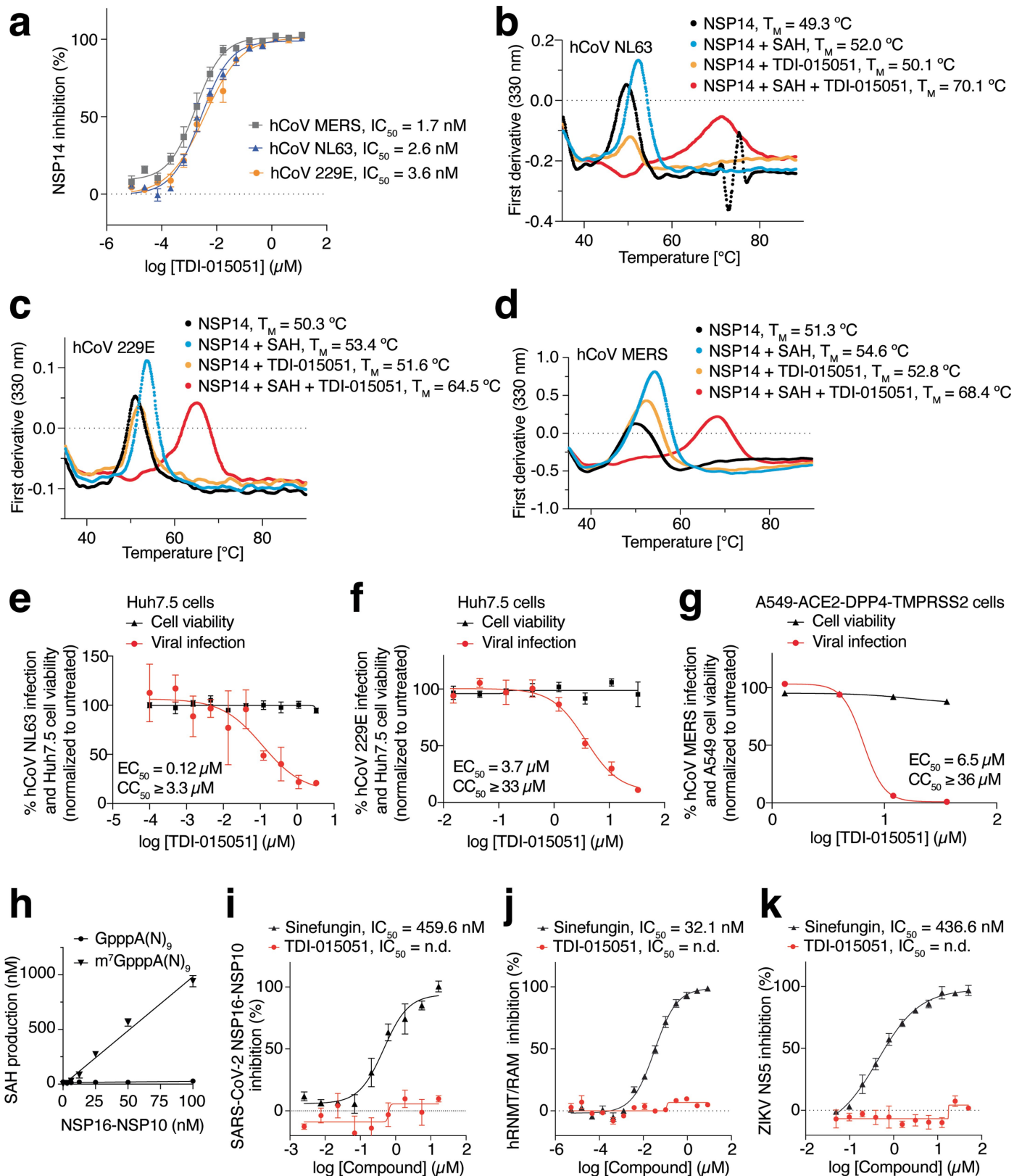


Extended Data Fig. 5 | See next page for caption.

Article

Extended Data Fig. 5 | Development of SARS-CoV-2 resistance mutations to TDI-015051 in Vero E6 cells. **a)** Representative gel images of SDS-PAGE analysis and Coomassie brilliant blue staining of purified full-length mutant NSP14 proteins. 2 µg total protein were loaded per sample. n = 2 biological replicates. For gel source data, see Supplementary Fig. 1. **b)** Thermal shift assay of wild-type and mutant NSP14 proteins (1 µM) binding to SAH (25 µM) and/or TDI-015051 (20 µM), respectively. n = 3 independent experiments; mean ± SD. **c)** Assessment of viral fitness of wild-type and NSP14-P335S plaque-purified viruses co-cultured starting at 10:0, 0:10, or 1:9 ratio

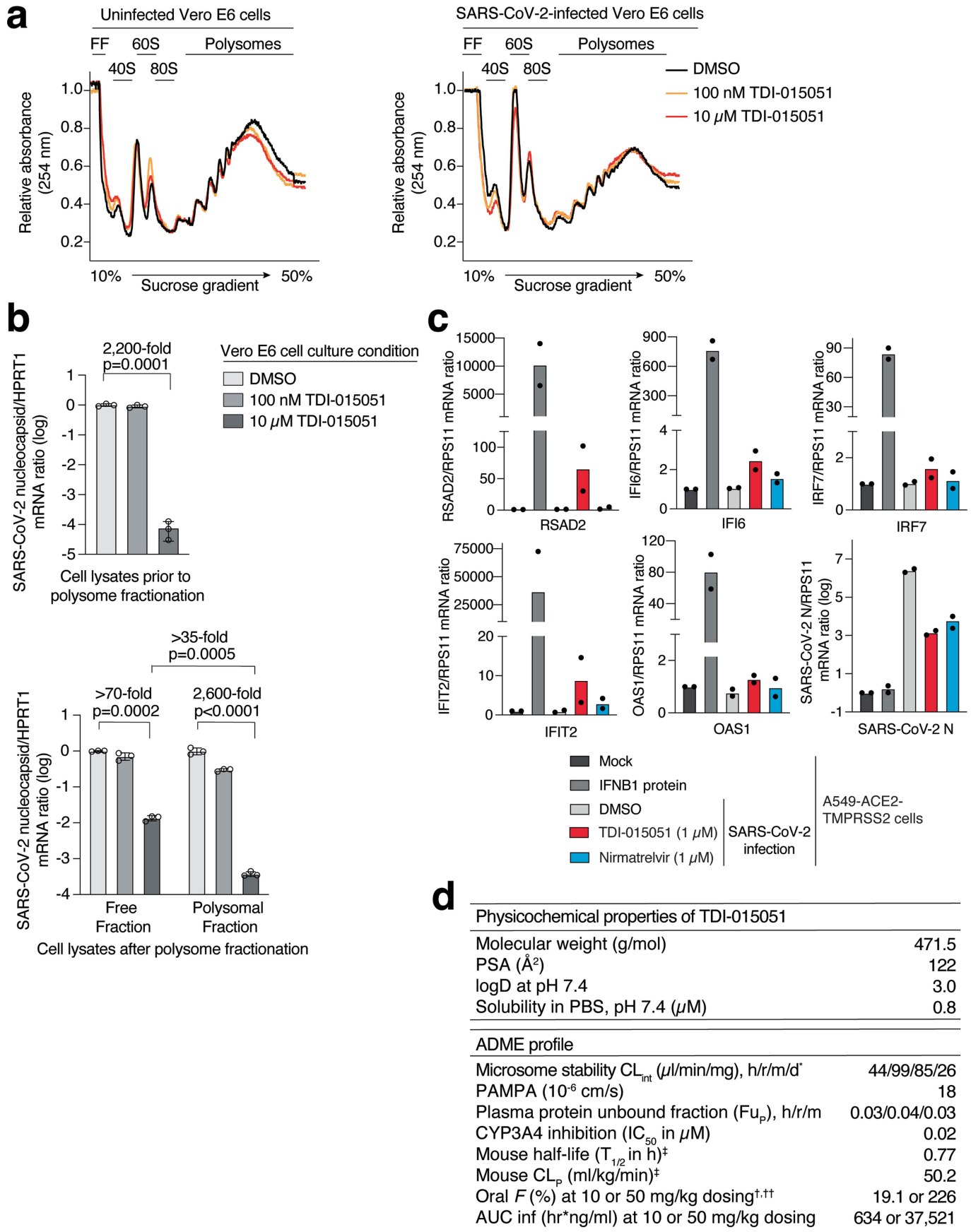
monitored over 2 passages in A549-ACE2-TMPRSS2 cells, respectively. n = 2 biological replicates. **d)** Antiviral activity of TDI-015051 against infectious clone-derived wild-type or NSP14-mutant SARS-CoV-2 viruses in Vero E6 cells. n = 3 independent experiments; mean ± SD. **e)** Antiviral activity of nirmatrelvir against infectious clone-derived wild-type or NSP14-mutant SARS-CoV-2 viruses in Vero E6 cells. n = 3 independent experiments; mean ± SD. **f)** Synergy distribution plot including summary synergy scores generated for TDI-015051 and nirmatrelvir co-dosed for inhibition of SARS-CoV-2 infection in Huh-7.5 cells using SynergyFinder3.0.



Extended Data Fig. 6 | See next page for caption.

Article

Extended Data Fig. 6 | Specificity of TDI-015051. **a)** Dose-dependent inhibition of the NSP14 MTase activity of β -hCoV-MERS, α -hCoV-NL63, or α -hCoV-229E (tested at 1.7 nM, 2 nM, or 1 nM enzyme, respectively) by TDI-015051 using the MTase GloTM assay. n = 3 independent experiments; mean \pm SD. **b-d)** Thermal melting profiles in first derivative mode of 1 μ M β -hCoV-MERS NSP14 (**b**), α -hCoV-NL63 NSP14 (**c**), or α -hCoV-229E NSP14 (**d**), alone or in presence of SAH (25 μ M) and/or TDI-015051 (20 μ M) recorded at 330 nm over a temperature gradient of 35 °C to 95 °C, respectively. Profiles are representative of 3 independent experiments. **e,f)** hCoV-NL63 (**e**) or hCoV-229E (**f**) antiviral activity and cytotoxicity of TDI-015051 in Huh-7.5 cells. n = 3 independent experiments; mean \pm SD. **g)** hCoV-MERS antiviral activity and cytotoxicity of TDI-015051 in A549-ACE2-DPP4-TMPRSS2 cells. Data are represented as mean values; n = 2. **h)** MTase Glo assay to compare the substrate specificity of the SARS-CoV-2 NSP16-NSP10 MTase complex towards GpppA(N)₉ or m'GpppA(N)₉, n = 3 independent experiments; mean \pm SD. **i)** Dose-dependent inhibition of the SARS-CoV-2 NSP16-NSP10 MTase complex by TDI-015051 and sinefungin. n = 3 independent experiments; mean \pm SD; n.d., not defined. **j)** Dose-dependent inhibition of the human RNMT-RAM MTase complex by TDI-015051 and sinefungin. n = 3 independent experiments; mean \pm SD; n.d., not defined. **k)** Dose-dependent inhibition of ZIKV NS5 MTase by TDI-015051 and sinefungin. n = 3 independent experiments; mean \pm SD; n.d., not defined.

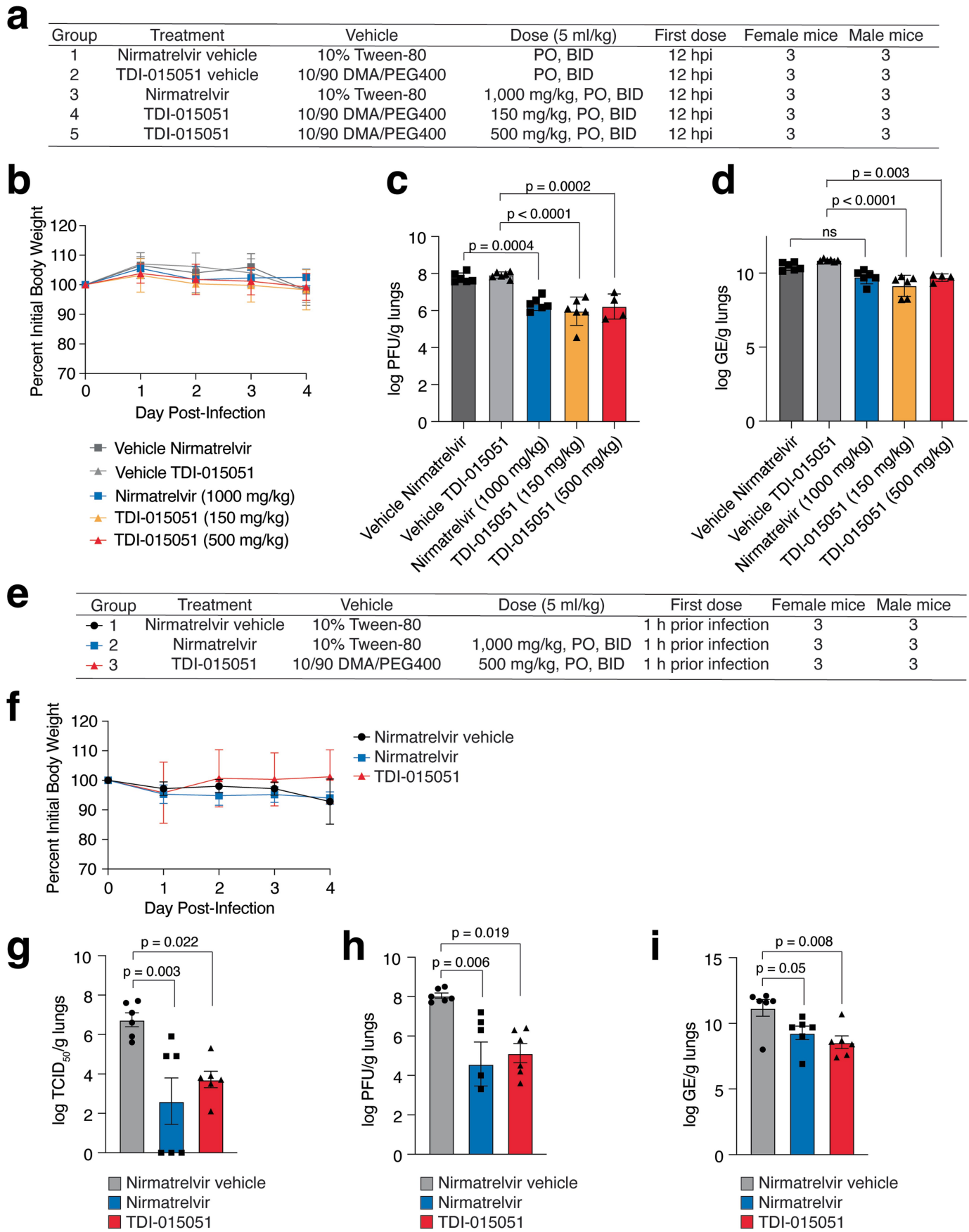


Extended Data Fig. 7 | See next page for caption.

Article

Extended Data Fig. 7 | Insights into the cellular mechanism of inhibition of SARS-CoV-2 replication by TDI-015051. **a)** Polysome profiling of uninfected (left panel) or SARS-CoV-2-infected (right panel) Vero E6 cells treated with TDI-015051 (100 nM or 10 μ M) or DMSO for 8 h, respectively. FF, free fraction. Profiles are representative of 2 independent experiments. **b)** Upper panel: Ratio of SARS-CoV-2 nucleocapsid mRNA relative to host HPRT1 in lysates of Vero E6 cells treated with TDI-015051 (100 nM or 10 μ M) or DMSO and infected with SARS-CoV-2 for 8 h, respectively, prior to polysome fractionation. Lower panel: Ratio of SARS-CoV-2 nucleocapsid mRNA relative to host HPRT1 in the free fraction or polysomal fraction of lysates of Vero E6 cells treated with TDI-015051 (100 nM or 10 μ M) or DMSO and infected with SARS-CoV-2 for 8 h, respectively, after polysome fractionation. $n = 3$; mean \pm SD. Adjusted p values by ordinary one-way ANOVA are given. **c)** Inhibition of SARS-CoV-2 replication

by TDI-015051 induced ISG expression in A549-ACE2-TMPRSS2 cells. Cells were either mock-infected or infected with SARS-CoV-2. Infected cells were pre-treated for 1 h with DMSO, TDI-015051 (1 μ M), or nirmatrelvir (1 μ M), respectively. Treatment of cells with IFNB1 protein (1 nM) served as positive control. Host and viral transcripts were quantified by RT-qPCR 24 h after SARS-CoV-2 infection. Data are represented as mean values; $n = 2$. **d)** Physicochemical and in vitro ADME (absorption, distribution, metabolism, and excretion) parameters of TDI-015051 and in vivo mouse pharmacokinetics. *Intrinsic clearance obtained from NADPH-treated liver microsomes. [†]Intravenous dosing performed at 5 mg/kg in CD-1 mice using a Cremophor-EL-based vehicle ($n = 3$). ^{††}PO dosing performed in PEG300-based solution formulation at 10 and 50 mg/kg, respectively, in CD1 mice ($n = 3$).



Extended Data Fig. 8 | See next page for caption.

Article

Extended Data Fig. 8 | Antiviral efficacy of TDI-015051 in a K18-hACE2 transgenic mouse model of SARS-CoV-2 infection. **a)** Design of TDI-015051 antiviral efficacy study in K18-hACE2 transgenic mice. Compound dosing started 12 hpi. PO, oral; BID, twice daily. **b)** Mice of all groups ($n = 6/\text{group}$) were monitored daily for body weight. $n = 3$; mean \pm SD. **c)** Plaque assays of clarified lung homogenate of mice were performed at 4 dpi of the therapeutic antiviral efficacy study. Numbers of viral infectious particles are graphed as \log_{10} PFU/g lung tissue. For groups 1–4: $n = 6$; for group 5: $n = 4$; mean \pm SD. **d)** Total RNAs of heat-inactivated lung homogenate supernatants were used for RT-qPCR of the SARS-CoV-2 E gene mRNA. Expression of E gene is given as \log_{10} viral genome equivalents/g lung tissue. For groups 1–4: $n = 6$; for group 5: $n = 4$; mean \pm SD. **e)** Design of the prophylactic TDI-015051-mediated antiviral efficacy study in K18-hACE2 transgenic mice. Compound dosing started 1 h before viral infection. PO, oral; BID, twice daily. **f)** Mice ($n = 6/\text{group}$) of the prophylactic antiviral efficacy study were monitored daily for body weight. **g)** Viral lung titers were determined at 4 dpi. Lung titers are graphed as \log_{10} TCID₅₀/g lungs. $n = 6$; mean \pm SD. **h)** Plaque assays of clarified lung homogenate were performed at 4 dpi. Numbers of viral infectious particles are graphed as \log_{10} PFU/g lungs. $n = 6$; mean \pm SD. **i)** Total RNAs of heat-inactivated lung homogenate supernatants of mice were used for RT-qPCR of the SARS-CoV-2 E gene. Gene expression (GE) of the E gene is given as \log_{10} of viral genome equivalents/g lung tissue. $n = 6$; mean \pm SD. Adjusted p values by ordinary one-way ANOVA are given in c-d, g-i.

Extended Data Table 1 | Data collection and processing statistics for the crystallographic structure of SARS-CoV-2 NSP14 in complex with SAH and TDI-015051

Ligand	TDI-015051
X-ray source	PXII/X10SA (SLS ¹)
Wavelength [Å]	1.0000
Detector	EIGER
Temperature [K]	100
Space group	P 2 ₁
Cell: a; b; c; [Å]	67.45; 101.07; 90.47
α; β; γ; [°]	90.0; 108.4; 90.0
Resolution [Å]	2.18 (2.41-2.18) ²
Unique reflections	41664 (2083)
Multiplicity	4.4 (3.9)
Spherical completeness [%]	69.5 (13.5)
Ellipsoidal completeness [%]	93.1 (60.7)
R _{pim} [%] ⁶	3.0 (49.3)
R _{sym} [%] ³	5.6 (86.5)
R _{meas} [%] ⁴	6.3 (99.8)
CC _{1/2} [%]	99.80 (57.60)
Mean(I)/sd ⁵	12.4 (1.5)

¹ SWISS LIGHT SOURCE (SLS, Villigen, Switzerland)

² values in parenthesis refer to the highest resolution bin.

$$^3 R_{sym} = \frac{\sum_h \sum_i^n |\hat{I}_h - I_{h,i}|}{\sum_h \sum_i^n I_{h,i}} \text{ with } \hat{I}_h = \frac{1}{n_h} \sum_i^n I_{h,i}$$

where $I_{h,i}$ is the intensity value of the i th measurement of h

$$^4 R_{meas} = \frac{\sum_h \sqrt{\frac{n_h}{n_h-1}} \sum_i^n |\hat{I}_h - I_{h,i}|}{\sum_h \sum_i^n I_{h,i}} \text{ with } \hat{I}_h = \frac{1}{n_h} \sum_i^n I_{h,i}$$

where $I_{h,i}$ is the intensity value of the i th measurement of h

⁵ calculated from independent reflections

$$^6 \text{Precision-indicating } R_{pim} = \frac{\sum_h \sqrt{\frac{1}{(N-1)} |I_{hl} - \langle I_h \rangle|}}{\sum_h \langle I_h \rangle}$$

Summary of the crystallographic analysis of the SARS-CoV-2 NSP14-SAHL-TDI-01051 ternary complex.

Article

Extended Data Table 2 | Refinement statistics for crystallographic structure of SARS-CoV-2 NSP14 in complex with SAH and TDI-015051

Ligand	TDI-015051
Resolution [Å]	65.51-2.18
Number of reflections (working /test)	40645 / 1019
R _{cryst} [%]	19.0
R _{free} [%]	24.4
Total number of atoms:	
Protein	6899
Water	191
Ligand	66
S-adenosyl-L-homocysteine	52
Imidazole	25
1,2-Ethanediol	8
Chloride	4
Zinc	7
Average B-factors	
Protein	68.0
Ligand	48.0
Water	54.0
Other atoms	61.5
Deviation from ideal geometry:	
Bond lengths [Å]	0.007
Bond angles [°]	1.50
Bonded B's [Å ²]	4.3
Ramachandran plot:	
Favoured [%]	96.77
Allowed [%]	3.11
Outliers [%]	0.12
Molprobity score	1.23
Molprobity clashscore	0.94

Statistics of the final structure and the refinement process for the SARS-CoV-2 NSP14-SAHL-TDI-01051 ternary complex are listed.

Reporting Summary

Nature Portfolio wishes to improve the reproducibility of the work that we publish. This form provides structure for consistency and transparency in reporting. For further information on Nature Portfolio policies, see our [Editorial Policies](#) and the [Editorial Policy Checklist](#).

Statistics

For all statistical analyses, confirm that the following items are present in the figure legend, table legend, main text, or Methods section.

n/a Confirmed

- The exact sample size (n) for each experimental group/condition, given as a discrete number and unit of measurement
- A statement on whether measurements were taken from distinct samples or whether the same sample was measured repeatedly
- The statistical test(s) used AND whether they are one- or two-sided
Only common tests should be described solely by name; describe more complex techniques in the Methods section.
- A description of all covariates tested
- A description of any assumptions or corrections, such as tests of normality and adjustment for multiple comparisons
- A full description of the statistical parameters including central tendency (e.g. means) or other basic estimates (e.g. regression coefficient) AND variation (e.g. standard deviation) or associated estimates of uncertainty (e.g. confidence intervals)
- For null hypothesis testing, the test statistic (e.g. F , t , r) with confidence intervals, effect sizes, degrees of freedom and P value noted
Give P values as exact values whenever suitable.
- For Bayesian analysis, information on the choice of priors and Markov chain Monte Carlo settings
- For hierarchical and complex designs, identification of the appropriate level for tests and full reporting of outcomes
- Estimates of effect sizes (e.g. Cohen's d , Pearson's r), indicating how they were calculated

Our web collection on [statistics for biologists](#) contains articles on many of the points above.

Software and code

Policy information about [availability of computer code](#)

Data collection	BioTek Gen5 Software was used to measure the luminescence readout during HTS.
Data analysis	SPR data were analyzed using the Biacore Insight Evaluation 3.0 software. RNA-seq data were analyzed using STAR-2.5.2a15. GraphPad Prism software (Version 10.1.1) was used for calculation of IC50, EC50, Km values and statistical tests. Structural data were processed using the programs autoPROC, XDS and autoPROC, AIMLESS. For solving crystal structures, the program Phaser was used. Subsequent model building and refinement was performed with COOT and the software package CCP445. The ligand parameterization and generation of the corresponding library files were carried out with CORINA. The Ramachandran plot of the final model calculated with Molprobity. For synergy studies, SynergyFinder 2.0 was used. For RNAseq data analysis, STAR-2.5.2a was used. Pharmacokinetic parameters were calculated using non-compartmental pharmacokinetic analysis supported by the PK solver Excel Add-in. For LC/MS data analysis, Skyline Daily v22 and Analyst software (version 1.6.2; Applied Biosystems Sciex) were used. For chemical library selection and preparation, Biovia pipeline pilot software and fingerprint-based (FCFP6) clustering software were used.

For manuscripts utilizing custom algorithms or software that are central to the research but not yet described in published literature, software must be made available to editors and reviewers. We strongly encourage code deposition in a community repository (e.g. GitHub). See the Nature Portfolio [guidelines for submitting code & software](#) for further information.

Data

Policy information about [availability of data](#)

All manuscripts must include a [data availability statement](#). This statement should provide the following information, where applicable:

- Accession codes, unique identifiers, or web links for publicly available datasets
- A description of any restrictions on data availability
- For clinical datasets or third party data, please ensure that the statement adheres to our [policy](#)

RNA sequencing data generated during the study are available on the NCBI Short-Read Archive (SRA) under the BioProject number PRJNA1035531. With regard to HTS data, structures of compounds, smiles strings and normalized percent inhibition data are downloadable in the Open Science Framework (https://osf.io/xk5uf/?view_only=01b3077a87cd495fb21e51e0dba4cf9f). X-ray crystallographic coordinates and structure factor files have been deposited at RCSB Protein Data Bank under accession number 8R7B.

Research involving human participants, their data, or biological material

Policy information about studies with [human participants or human data](#). See also policy information about [sex, gender \(identity/presentation\), and sexual orientation](#) and [race, ethnicity and racism](#).

Reporting on sex and gender N/A, this study did not involve human research subjects.

Reporting on race, ethnicity, or other socially relevant groupings N/A, this study did not involve human research subjects.

Population characteristics N/A, this study did not involve human research subjects.

Recruitment N/A, this study did not involve human research subjects.

Ethics oversight N/A, this study did not involve human research subjects.

Note that full information on the approval of the study protocol must also be provided in the manuscript.

Field-specific reporting

Please select the one below that is the best fit for your research. If you are not sure, read the appropriate sections before making your selection.

Life sciences Behavioural & social sciences Ecological, evolutionary & environmental sciences

For a reference copy of the document with all sections, see nature.com/documents/nr-reporting-summary-flat.pdf

Life sciences study design

All studies must disclose on these points even when the disclosure is negative.

Sample size No sample size calculation was performed. We utilized sample sized as used in similar studies (Owen et al., 2021).

Data exclusions For our in-vivo efficacy study, when compounds were dosed 12 hours post infection, two animals from group 5 (5-1F and 5-2F) were euthanized early (Day 3) due to meeting humane euthanasia criteria. Animals were lethargic following dosing and blood collection likely due to the volume of blood collected and potential stress from handling as these mice were on the smaller side. We did perform viral quantification on these two animals and this data is included in the tables, but they have been excluded from any analysis.

Replication Unless otherwise stated, all assays were performed at least in triplicates. The HTS pilot screen was replicated at two different days and showed excellent reproducibility with an R2 value of 0.95. This high degree of reproducibility allowed us to screen the entire compound library once without replication). False positive or false negative hits were eliminated subsequently by performing validation experiments.

Randomization Mice were assigned to experimental groups randomly. Besides animal work, randomization was not relevant to this study.

Blinding As this is an observational study, investigators were not blinded. No measure was subjective.

Reporting for specific materials, systems and methods

We require information from authors about some types of materials, experimental systems and methods used in many studies. Here, indicate whether each material, system or method listed is relevant to your study. If you are not sure if a list item applies to your research, read the appropriate section before selecting a response.

Materials & experimental systems

n/a	Involved in the study
<input type="checkbox"/>	<input checked="" type="checkbox"/> Antibodies
<input type="checkbox"/>	<input checked="" type="checkbox"/> Eukaryotic cell lines
<input checked="" type="checkbox"/>	<input type="checkbox"/> Palaeontology and archaeology
<input type="checkbox"/>	<input checked="" type="checkbox"/> Animals and other organisms
<input checked="" type="checkbox"/>	<input type="checkbox"/> Clinical data
<input type="checkbox"/>	<input checked="" type="checkbox"/> Dual use research of concern
<input checked="" type="checkbox"/>	<input type="checkbox"/> Plants

Methods

n/a	Involved in the study
	<input checked="" type="checkbox"/> ChIP-seq
	<input checked="" type="checkbox"/> Flow cytometry
	<input checked="" type="checkbox"/> MRI-based neuroimaging

Antibodies

Antibodies used

SARS-CoV-2 (COVID-19) nucleocapsid (N) antibody, Genetex, GTX135357; MERS-CoV nucleocapsid-specific antibody, SinoBiological, 40068-MM10

Validation

SARS-CoV-2 (COVID-19) nucleocapsid (N) antibody: Antibody validated for IP, WB, ICC/IF; Reactivity towards SARS Coronavirus, SARS Coronavirus 2. C Di Primio et al. PNAS Nexus 2023; 2 (9) : pgad282 Severe acute respiratory syndrome coronavirus 2 infection leads to Tau pathological signature in neurons; N Schmidt et al. Cell 2023; SND1 binds SARS-CoV-2 negative-sense RNA and promotes viral RNA synthesis through NSP9. Manufacturer statement for MERS-CoV nucleocapsid-specific antibody: The antibody reacts with MERS-CoV (NCoV / Novel coronavirus) Nucleocapsid protein (NP protein). Validated applications: WB, ELISA

Eukaryotic cell lines

Policy information about [cell lines](#) and [Sex and Gender in Research](#)

Cell line source(s)

Vero E6 cells (Chlorocebus sabaeus; sex: female, kidney epithelial, ATCC, CRL-1586) obtained from Ralph Baric (University of North Carolina at Chapel Hill), Caco-2 cells (Homo sapiens; sex: male, colon epithelial) were obtained from the ATCC (HTB-37™), and Huh-7.5 hepatoma cells (Homo sapiens; sex: male, liver epithelial), were generated from Huh-7 cell s (Blight et al., 2002). A549-ACE2-TMPRSS2 cells were generated from commercially available A549 cells (Homo sapiens; sex: male, lung epithelial, CCL-185, ATCC). SmallAir, an in vitro primary cell model of human small airway epithelium from a healthy donor (no smoker without known pathology), was purchased from Epithelix (EP21SA).

Authentication

Cell lines were either purchased from commercial vendors and/or regularly visually checked for morphology.

Mycoplasma contamination

All cell lines have regularly been tested negative for contamination with mycoplasma.

Commonly misidentified lines (See [ICLAC](#) register)

A549 cells. To test our NSP14 inhibitor in cells of lung origin, we assessed its SARS-CoV-2 antiviral activity first in A549 cells, a human adenocarcinomic alveolar basal epithelial cell line.

Animals and other research organisms

Policy information about [studies involving animals](#); [ARRIVE guidelines](#) recommended for reporting animal research, and [Sex and Gender in Research](#)

Laboratory animals

CD-1 female mice (22 - 25 g) were used for PK studies. For efficacy studies, male and female (n = 3/sex/group) 6-8 week old, transgenic K18-hACE2 mice were used. Mice were housed in a temperature (20-23 °C) and humidity (30-70%)controlled room on a 12 hour light / 12 hour dark schedule.

Wild animals

The study did not involve wild animals.

Reporting on sex

Mice were selected because they represent the lowest ordered species that are routinely used for efficacy evaluation of antiviral compounds against coronavirus infection. Only female mice were be used for PK profiling until confirmation of the efficacy PK due to the reduced cost burden of housing of female mice compared to male mice. For in vivo mouse efficacy studies, male and female (n = 3/sex/group) 6-8 week old, transgenic K18-hACE2 mice were used.

Field-collected samples

This study did not involve samples collected from the field.

Ethics oversight

All animal studies were ethically reviewed and carried out in accordance with European Directive 2010/63/EU and the GSK Policy on the Care, Welfare and Treatment of Animals. All animal procedures described in this study have been approved by the Institutional Animal Care and Use Committee (IACUC) at HMH-Center for Discovery and Innovation.

Note that full information on the approval of the study protocol must also be provided in the manuscript.

Dual use research of concern

Policy information about [dual use research of concern](#)

Hazards

Could the accidental, deliberate or reckless misuse of agents or technologies generated in the work, or the application of information presented in the manuscript, pose a threat to:

No	Yes
<input checked="" type="checkbox"/>	<input type="checkbox"/> Public health
<input checked="" type="checkbox"/>	<input type="checkbox"/> National security
<input checked="" type="checkbox"/>	<input type="checkbox"/> Crops and/or livestock
<input checked="" type="checkbox"/>	<input type="checkbox"/> Ecosystems
<input checked="" type="checkbox"/>	<input type="checkbox"/> Any other significant area

Experiments of concern

Does the work involve any of these experiments of concern:

No	Yes
<input checked="" type="checkbox"/>	<input type="checkbox"/> Demonstrate how to render a vaccine ineffective
<input type="checkbox"/>	<input checked="" type="checkbox"/> Confer resistance to therapeutically useful antibiotics or antiviral agents
<input checked="" type="checkbox"/>	<input type="checkbox"/> Enhance the virulence of a pathogen or render a nonpathogen virulent
<input checked="" type="checkbox"/>	<input type="checkbox"/> Increase transmissibility of a pathogen
<input checked="" type="checkbox"/>	<input type="checkbox"/> Alter the host range of a pathogen
<input checked="" type="checkbox"/>	<input type="checkbox"/> Enable evasion of diagnostic/detection modalities
<input checked="" type="checkbox"/>	<input type="checkbox"/> Enable the weaponization of a biological agent or toxin
<input checked="" type="checkbox"/>	<input type="checkbox"/> Any other potentially harmful combination of experiments and agents

Precautions and benefits

Biosecurity precautions	All experiments were conducted in a Biosafety Level 3 (BSL-3) facility.
Biosecurity oversight	Prior to conducting this work, the protocol was reviewed and approved by The Rockefeller University's Institutional Biosafety Committee (IBC).
Benefits	Understanding the mutations that confer resistance are critical for the development of viral methyltransferase inhibitors.
Communication benefits	Communication of these results provides essential insights into the development of next generation MTase inhibitors.

Plants

Seed stocks	Does not apply to this study.
Novel plant genotypes	Does not apply to this study.
Authentication	Does not apply to this study.